International Journal of Plasticity 133 (2020) 102806

Contents lists available at ScienceDirect

International Journal of Plasticity

journal homepage: http://www.elsevier.com/locate/ijplas

Extraordinary room temperature tensile ductility of laminated Ti/Al composite: Roles of anisotropy and strain rate sensitivity

Wenhuan Chen, Weijun He *, Zejun Chen, Bin Jiang, Qing Liu

College of Materials Science and Engineering, Chongqing University, Chongqing, 400044, China

ARTICLE INFO

Keywords:
Laminated metal composites
Ductility
Strengthening
Anisotropy
Deformation mechanism

ABSTRACT

Al/Ti/Al laminated metal composites (LMCs), with layer thicknesses ≥800 μm, were fabricated via hot rolling bonding and annealing. The fabricated Al/Ti/Al LMCs displayed improved tensile ductility compared with both the single Ti and single Al layers. Combinational analyses based on digital image correlation and finite element modeling revealed that the width of the interface affected zones (IAZ) could exceed 150 μm, which is more than one order of magnitude larger than previously reported values. The mismatch of plastic anisotropy between the Ti layer and the Al layer may play a crucial role in realizing such a wide IAZ. Slip trace analysis indicated that more pyramidal and basal slips were activated at the Ti/Al interface than in the central part of the Ti layer, which may be attributed to the complex stress/strain state in the IAZ. Although a wide IAZ was observed, the strain hardening capability of the Al/Ti/Al LMCs did not obviously improve. In contrast, the strain rate sensitivity improved, which is assumed to play a key role in the improved ductility of the Al/Ti/Al LMCs. This study can provide a direction for the design of hetero-structured materials with high strength and high ductility.

1. Introduction

The fabrication of metallic materials that are both strong and ductile has been a topic of intense interest in the field of materials science and engineering. Generally, metallic materials can be strengthened via the controlled introduction of defects in the homogeneous matrix, e.g., by using alloying elements and with a high density of internal boundaries (Lu, 2010; Lu et al., 2009). However, the increased strength realized using such strategies is often accompanied by a sharp loss in ductility. To overcome this trade-off between strength and ductility, researchers have turned to the natural world for inspiration. Natural (biological) materials, such as bamboo (Habibi et al., 2015), shell (Heinemann et al., 2011; Jiao et al., 2015), tooth (Yilmaz et al., 2015), and bone (Tertuliano and Greer, 2016) generally feature heterogeneous structures, which are understood to be key factors in achieving excellent mechanical properties (Liu et al., 2017).

Inspired by the hierarchical structure of natural materials, increasing attention has been paid to heterogeneous metallic materials, such as gradient (Cheng et al., 2018; Fang et al., 2011; Lu, 2014), laminated (Inoue et al., 2008; Li et al., 2019a; Seok et al., 2016), bi-modal (Sitarama Raju et al., 2013; Zhu and Lu, 2012), and harmonic (Park et al., 2018) materials. Compared with their homogeneous counterparts, many heterogeneous metallic materials were reported to show a superior combination of strength and ductility (Hasan et al., 2019; Wang et al., 2018a, 2018c). The microstructures of heterogeneous metallic materials are generally comprised of

* Corresponding author.
E-mail address: weijun.he@cqu.edu.cn (W. He).

https://doi.org/10.1016/j.ijplas.2020.102806
Received 24 February 2020; Received in revised form 29 May 2020; Accepted 30 May 2020
Available online 15 June 2020

multiple domains with remarkably different mechanical properties (Wu and Zhu, 2017). The inter-domain transition may be sharp or in the form of a gradient. During loading, on one side, the various domains deform in different ways because of the different microstructures. Furthermore, deformations between the different domains influence each other because of the constraints of inter-domain transition, supposing that the inter-domain transition portion can bear a sufficiently high stress or/and deformation. Compatible deformation between the different domains can significantly reshape the applied strain path or/and stress state, which provides an opportunity to realize significant strengthening and strain hardening; this characteristic has been recognized as a key one for heterostructured materials (Hasan et al., 2019; Wu et al., 2014a, 2014b). For example, graded materials with a fine grain near the surface and coarser grains in the core region were reported to possess an excellent combination of strength and ductility compared with their counterparts with a uniform grain size (Lin et al., 2018; Yang et al., 2015; Yin et al., 2016). The main underlying mechanism was related to additional work hardening, which resulted from the formation and storage of geometry necessary dislocations (GNDs) induced via the microscopic strain gradient caused by a gradient in the grain size (Ashby, 1970; Li et al., 2017; Shao et al., 2018; Wu et al., 2014a).

Compared with graded materials, laminated materials, which are characterized by bonded alternating layers, are relatively simple to fabricate, e.g., by bonding and deposition. Therefore, laminated materials are one kind of ideal model material for the investigation of heterostructured materials. The various layers with different microstructures and mechanical properties can be recognized as different domains. The tensile behavior of laminated materials is significantly influenced by the layer thickness and the interface. For the tensile yield stress of laminated materials with thin layers (with thickness roughly smaller than 1 μm but larger than 1.5 nm) and a sharp interface, a classic Hall-Petch relationship has often been observed with change of the laminate spacing (Chen et al., 2020; Lesuer et al., 1996; Nizolek et al., 2016). For laminated materials with thick layers (>50 μm) and a sharp interface, the tensile yield stress was assumed to be readily predicted by the rule of mixtures (Kim and Hong, 2013; Lesuer et al., 1996; Ma et al., 2015). The tensile elongation of thick laminated materials was often observed to be lower than that predicted by the rule of mixtures (Wang et al., 2015; Wu et al., 2015; Zhu et al., 2019b) because of interface delamination or/and early cracking in the less ductile layer. It was recently reported that when a gradient transition zone formed between different domains or the layer thickness was between 1 and 50 μm, strengthening above that expected by the rule of mixtures and a high strain hardening rate could be obtained in coarse/ultrafine grained copper (Wang et al., 2019a), Ti/Al (Du et al., 2016) and coarse/ultrafine grained Cu–Zn (Wang et al., 2019b). The tensile ductility of the laminated Ti/Al composite was higher than both the monolithic Ti and monolithic Al (Huang et al., 2018b). Interface affected zones (IAZ), which formed as a result of compatible deformation between different layers, were reported to play a key role in the high strength and high ductility of laminated materials (Huang et al., 2018a; Ma et al., 2016). The accumulation of GNDs at the IAZ resulted in extra back stress strengthening and an enhanced strain hardening rate (Huang et al., 2018a; Ma et al., 2016), which contributed to the strengthening and the excellent ductility.

In spite of the above mentioned progress, the deformation behaviors of laminated materials are still far from clear. For example, the possible influence of the layered structure on the deformation mechanisms (activation of slip systems) has not been discussed in detail in previous studies. The activation of different slip systems (prismatic, basal or pyramidal slip system for instance in Ti) or twinning systems were expected to significantly affect the strength and ductility of metallic materials. In addition, the formation of a strain gradient at the interface affected zones has often been explained by the discrepancies in the elastic limit and the potential for stable plastic deformation of the different layers. However, plastic deformation causing asynchronism between the different layers may only cause an effective strain gradient during the early stage of the entire deformation. The discrepancies for stable plastic deformation cannot explain the extraordinary tensile ductility reported in Ti/Al laminated materials (Huang et al., 2018b); hence, new mechanisms need to be explored. Moreover, a strong texture is often formed during plastic forming, which will generally induce obvious anisotropic plastic deformation in subsequent loading. Whether texture induced anisotropy has an effect on the deformation of laminated materials has not previously been addressed. Therefore, significant work remains to be done to explore the deformation behavior of laminated materials.

In this work, thick Al/Ti/Al laminated composites, with layer thicknesses ≥800 μm, were fabricated via hot rolling bonding. The slip trace method based on ex-situ scanning electron microscopy and electron backscatter diffraction characterization was used to investigate the effect of the layered structure on the deformation mechanism. The digital image correction technique was used to analyze the strain distribution. Finite element simulations were performed to explore the effect of texture on the deformation of Al/Ti/Al. It was found that the extraordinary room temperature tensile ductility of Al/Ti/Al was closely related to the discrepancy of the texture induced plastic anisotropy between the constituent layers. The results of this work can be beneficial for further investigation and fabrication of heterostructured materials with a high strength and extraordinarily high ductility.

2. Experimental materials and methods

2.1. Materials preparations

Commercial pure titanium (TA2) and aluminum (1060) sheets with an initial thickness of 1.4 mm and 3 mm, respectively, were selected as raw materials to fabricate Al/Ti/Al laminated metal composites (LMCs). The as-received Ti and Al sheets were cut into 60 mm (along rolling direction, RD) × 40 mm (along transverse direction, TD) sheets and then etched by 15 vol% HF and 10 vol% NaOH solutions, respectively, to remove the oxide on the surface. The cleaned sheets were stacked in the sequence of Al/Ti/Al as a sandwich billet. The Al/Ti/Al billets were preheated at 400 °C for 15 min. Then, Al/Ti/Al LMCs were fabricated by hot rolling bonding. The rolling direction was along the initial RD of the raw material. The rolling reduction was 45% and accomplished in a single pass. A rolling reduction of 45% was chosen to make sure that the Ti layer and the Al layer could be successfully bonded together, as

determined in our previous study (Chen et al., 2019). To obtain materials in different states (deformed or recrystallized), the Al/Ti/Al LMCs were annealed at 200, 300, 400, 500, and 600 °C for 1 h. The highest annealing temperature (600 °C) was selected to make sure that the Ti layer as well as the Al layer in the Al/Ti/Al LMCs could be fully recrystallized.

For comparison, monolithic Ti and monolithic Al sheets, which were subjected to the same thermo-mechanical treatments as the Al/Ti/Al LMCs, were also prepared. Monolithic Ti and monolithic Al sheets were fabricated by performing the same rolling and annealing, except that a separator was added between the Ti layer and the Al layer in the Al/Ti/Al billet. After rolling and annealing, the monolithic Ti and monolithic Al sheets could be separated from the Al/Ti/Al plate.

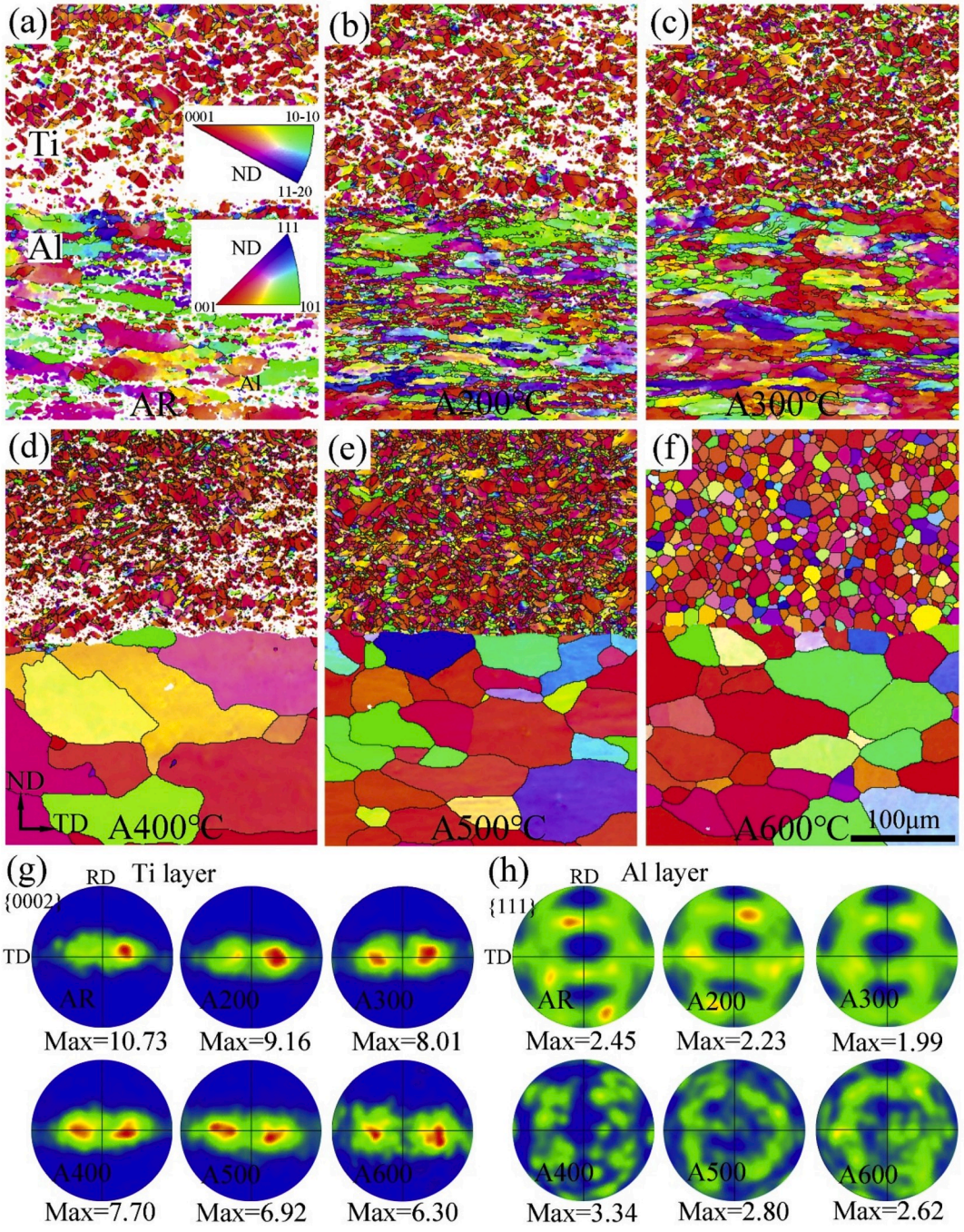

Fig. 1. Microstructures of the Al/Ti/Al LMCs after annealing at various temperatures: (a) as-rolled (AR), (b) A200, (c) A300, (d) A400, (e) A500, and (f) A600. Pole figures of the Al/Ti/Al LMCs after annealing at various temperatures: (g) Ti layer and (h) Al layer.

2.2. Mechanical properties and microstructure characterizations

A field-emission scanning electron microscope (SEM, MIRA3-TESCAN) equipped with an HKL electron backscatter diffraction (EBSD) detector was used to characterize the microstructures and texture of the Al/Ti/Al LMCs. The observed regions were on the transverse direction-normal direction (TD-ND) planes, which were ground and electro-polished using an electrolyte composed of methanol (60%), n-butanol (34%), and perchloric acid (6%). The step size for the EBSD data was 1 μm.

Uniaxial tensile tests at room temperature were carried to evaluate the mechanical properties of the fabricated Al/Ti/Al LMCs, monolithic Ti, and monolithic Al sheets. Dog-bone tensile samples with a gauge area of 12 (length) × 6 (width) mm were used. The tensile direction was along the TD. Tensile tests were performed on a universal testing machine (SHIMADZU SPL-10 kN) with an initial strain rate of $\sim 10^{-3}\ s^{-1}$. A non-contact laser extensometer was used to measure the strain. To ensure the reliability of the mechanical data, the tensile tests were repeated at least thrice for each sample.

To reveal the deformation mechanisms of the Al/Ti/Al LMCs, ex-situ SEM and EBSD characterizations were performed for the Al/Ti/Al LMCs annealed at 600 °C after application of tension along the TD. Before tension, the TD-ND plane of the dog-bone tensile sample was carefully ground, electro-polished, and characterized via SEM and EBSD. Then, the tension was interrupted at nominal strains of 0.5%, 3%, 7%, and 12%, followed by further microstructure characterization using SEM and EBSD. The tensile strain rate was $\sim 10^{-3}\ s^{-1}$. After the introduction of tension, no further grinding and polishing was carried out before microstructure observation. Four local regions (Ti/Al interface nearby region, the central region of the Ti layer, and the Al layer) were observed. The slip trace method (Zhu et al., 2019a) was used to analyze the activated slip systems. For comparison, ex-situ SEM and EBSD characterizations were also performed for the monolithic Ti sheet.

2.3. Strain distribution evaluation

To reveal the local strain distribution of the Al/Ti/Al LMCs, monolithic Ti, and monolithic Al during tensile deformation, digital image correlation (DIC) was applied on the TD-ND plane of the dog-bone tensile sample. Before the tensile experiment, black and white speck markers were carefully sprayed on the surface of the samples, acting as indicators for the DIC analysis. A CCD camera was used to record images at different strains. The two-dimensional strain distribution on the observed plane was calculated based on the relative displacement of different material points.

3. Experimental results

3.1. Microstructures of Al/Ti/Al LMCs

The Ti layer and the Al layer were bonded together after rolling bonding. In the Al/Ti/Al LMCs, the thickness of the Ti layer and Al layer were ~800 μm and ~1600 μm, respectively. Hence, the fabricated Al/Ti/Al LMCs was a type of thick laminated composite (Lesuer et al., 1996), which is generally easier to fabricate than thin laminated composites.

The EBSD microstructure of the as-rolled (AR) and the annealed Al/Ti/Al LMCs are shown in Fig. 1. In the EBSD image, the grains are colored according to their crystal orientation (also denoted as an IPF map), and the region with a white color is non-indexed because of the heavy crystal lattice distortion. The black solid line marks the grain boundary. Fig. 1 shows that: (1) the index rate in the AR sample was very low as a result of the large rolling deformation; (2) partial recrystallization occurred in the Al layer after annealing at 200 °C and 300 °C, while full recrystallization was realized at annealing temperatures ≥400 °C; (3) for the Ti layer, the ratio of the recovered (or partially recrystallized) area fraction increased with annealing temperature and full recrystallization was realized when the annealing temperature reached 600 °C.

Inoue et al. (2008) reported that the mechanical contrasts (tensile strength ratio and hardening exponent) between the constituent layers played a crucial role in optimizing the ductility of the multilayered steel composites. Liang et al. (2019) found that pre-stored dislocations may weaken the interface coupling effect in the Ni/Cu/Ni sandwich-structured composites. In the current study, Al/Ti/Al LMCs with different degrees of recrystallization in the Ti layer and Al layer, and thus different mechanical contrasts and dislocation densities between constituent layers, were fabricated by annealing at different temperatures. These materials could be used to evaluate the effects of the mechanical contrast or pre-stored dislocations between the constituent layers on the properties of Al/Ti/Al LMCs.

Fig. 1(g) shows the {0002} pole figures of the Ti layer in the Al/Ti/Al LMCs after annealing at different temperatures. For all samples, the Ti layer exhibited a typical bimodal basal texture with the *c-axis* oriented along the ND and tilting ±20–40° toward the TD, which is a very common texture in rolled α-Ti (Wang et al., 2018b). With increasing annealing temperature, the intensity of the bimodal basal texture gradually decreased. However, after annealing at the highest temperature (600 °C), the bimodal basal texture was still evident, which may cause strong anisotropy (Inagaki, 1992). To obtain relatively reliable pole figures for the Al layer in the Al/Ti/Al LMCs, a new set of EBSD images that include >400 grains in each map were obtained. The {111} pole figures of the Al layer after various annealing treatments are shown in Fig. 1(h). Brass {110}<112> and Copper {112}<111> were the main texture components in samples AR, A200, and A300. As the annealing temperature was increased to ≥400 °C, full recrystallization occurred and the Al layers exhibited a relatively weak texture.

3.2. Strength during tension

The tensile engineering stress-strain curves of Al/Ti/Al LMCs, monolithic Ti, and monolithic Al are presented in Fig. 2. In addition,

according to the rule of mixtures (ROM) based on the iso-strain assumption, the strength of the LMCs can be estimated by Lesuer et al. (1996):

$$\sigma = \sigma_{Ti}{}^{*}\nu_{Ti} + \sigma_{Al}{}^{*}\nu_{Al}, \quad (1)$$

*wh*ere σ, σ_{Ti}, and σ_{Al} are the flow strength of the LMCs, Ti layer, and Al layer, respectively, and ν_{Ti} and ν_{Al} are the cross-sectional area fraction of the Ti layer and Al layer, respectively. In the current study, it is reasonable to assume that the mechanical properties of the Ti layer and the Al layer in the Al/Ti/Al LMC are identical to the monolithic Ti and monolithic Al because they experienced the same thermo-mechanical process. In addition, as reported in our previous work as well as in other studies (Chen et al., 2019; Du et al., 2016), an intermetallic layer ($TiAl_3$) formed during the rolling bonding and annealing; however, it was very thin in this work (~1 μm for the A600 sample). After evaluation, the contribution of the $TiAl_3$ layer to the overall strength of Al/Ti/Al LMC was small enough that it could be ignored in the current study. The calculated stress-strain curves for the Al/Ti/Al LMC based on the ROM are also shown in Fig. 2.

Fig. 2 shows that: (1) the strength of the Al/Ti/Al LMCs, monolithic Ti, and monolithic Al decreased with increasing annealing temperature because of recovery and recrystallization; (2) full recrystallization resulted in a rapid strength decrease for the monolithic Ti and monolithic Al; (3) the Ti layer contributed more than the Al layer to the strength of the Al/Ti/Al LMCs; (4) for the Al/Ti/Al LMCs, the experimental strengths were always higher than the calculated values based on the ROM.

The mentioned positive discrepancy (extra strengthening) between the experimental results and the calculated strength based on the ROM has been previously reported for other layered composites (Du et al., 2016; Liang et al., 2019; Wang et al., 2019b). The additional strengthening above that expected from the ROM in layered materials is generally attributed to the interface coupling induced back stress strengthening and storage of geometry necessary dislocations (GNDs) (Huang et al., 2018a; Ma et al., 2016). Moreover, in the current study, the extra strengthening may also have been caused by extra activation of pyramidal slip (with high critical resolved shear stress) in the Ti layer of Al/Ti/Al LMCs compared with monolithic Ti, and this will be further discussed in section 3.5. Moreover, the magnitude of the extra strengthening (yield stress) in samples AR and A200 seems to be lower than that in the other samples, as indicated in Fig. 2. This may be attributed to the high dislocation density in the Al layer introduced by rolling that would decrease the pile-up distance of GNDs and weaken the interface coupling effect (Liang et al., 2019).

3.3. Tensile elongation

A more important phenomenon depicted in Fig. 2 is that the fracture elongation of the Al/Ti/Al LMCs was always higher (extra ductility) than both the monolithic Ti and monolithic Al regardless of the annealing temperature. This is interesting because the ductility of thick laminated composites have been reported to be lower than that of the constituent materials (Lesuer et al., 1996; Wang et al., 2015; Wu et al., 2015; Zhu et al., 2019b). A similar phenomenon (the fracture elongation of LMCs is higher than both the monolithic Ti and monolithic Al) was also reported in multi-layered Ti/Al composites in recent work (Huang et al., 2018b), in which

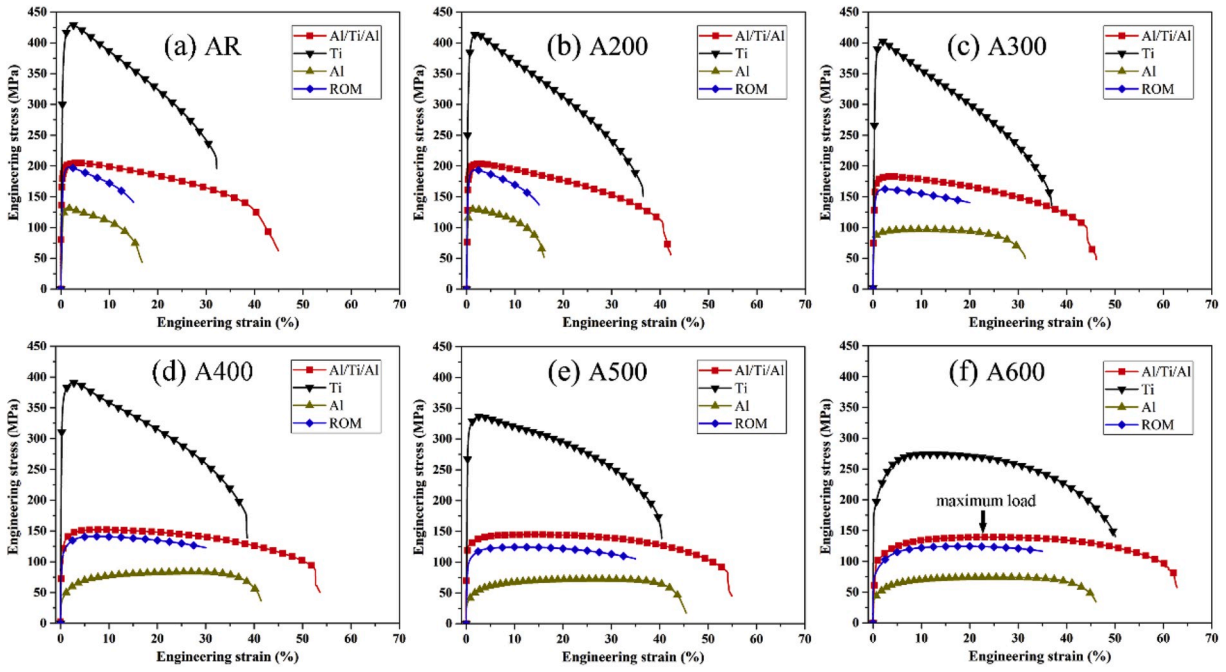

Fig. 2. Experimental and calculated (based on the rule of mixtures, ROM) uniaxial tensile engineering stress-strain curves of the Al/Ti/Al LMCs, monolithic Ti, and monolithic Al after annealing at various temperatures: (a) AR, (b) A200, (c) A300, (d) A400, (e) A500, and (f) A600.

the thickness of the layer was ~100 μm. To further reveal the effect of the layer structure on the tensile ductility, the evolution of the fracture elongation, uniform elongation, and post-necking elongation with annealing temperature were investigated, as shown in Fig. 3. The average fracture elongation of the monolithic Ti was actually higher than that of the monolithic Al, except for the A400 and A500 samples, as indicated in Fig. 3(a). For the A400 and A500 samples, full recrystallization occurred in Al, while a low degree of recovery or/and recrystallization occurred in Ti, as shown in Fig. 1.

The uniform elongation is completely different from fracture elongation. When the annealing temperature was equal to or lower than 200 °C, the uniform elongation of Al/Ti/Al LMCs was a little higher than that of the monolithic Ti and monolithic Al. When the annealing temperature was higher than 200 °C, Fig. 3(b) indicates that the uniform elongation of Al/Ti/Al LMCs was higher than that of monolithic Ti but lower than that of the monolithic Al. Generally, the excellent ductility of the layered composite can be attributed to the improved uniform elongation, which is enhanced by the higher strain hardening rate caused by the interface coupling effect (Huang et al., 2018a; Ma et al., 2016). However, in the current study, the uniform elongation of the Al/Ti/Al LMCs was not the highest even though it displayed the best tensile ductility in the A300, A400, A500, and A600 samples.

In addition, the strain hardening rate curves for all the samples during the uniform deformation stage are shown in Fig. 4. For comparison, the calculated strain hardening rate curves based on the ROM and simple average are also presented in Fig. 4. The strain hardening rate of the Al/Ti/Al LMCs was not the highest, and it was even lower than the expected values based on the ROM and simple average in some samples; hence, the results contradict previous reports of the Ti/Al LMCs having the highest strain hardening rate (Huang et al., 2018b). This may be related to the thicker layers in the current study. It has been reported that the initial strain hardening parameter is always inversely proportional to the layer spacing (Verdier et al., 2006). Nevertheless, in the current study, the extra ductility of the Al/Ti/Al LMCs cannot be explained by the interface coupling enhanced uniform elongation and strain hardening rate; hence, other mechanisms need to be further explored. For the AR and A200 samples, although the uniform elongation of the Al/Ti/Al LMCs was a little higher than the constituent materials, the amplitude of the improved uniform elongation (~1%) was too low to cause improved fracture elongation (~10%).

The post-necking elongation of the Al/Ti/Al LMCs (Fig. 3(c)) was higher than both the monolithic Ti and monolithic Al, which showed the same improvement trend as the fracture elongation. In addition, the proportion of post-necking elongation to fracture elongation was always higher than that for the uniform elongation. Therefore, the improved post-necking elongation in the Al/Ti/Al LMCs may play an important role in the improved tensile ductility. The post-necking elongation is often related to the strain rate sensitivity of materials (Ghosh, 1977). The strain rate sensitive parameters of the Al/Ti/Al LMCs, monolithic Ti, and monolithic Al and their relationship with the improved fracture elongation will be further discussed in section 5.2.

In addition to the extra strengthening beyond that expected from the ROM, the improved tensile ductility (fracture elongation) was more pronounced in the fabricated thick Al/Ti/Al LMCs. Therefore, the following results and discussion will focus on the ductility. Furthermore, the trend for the improved tensile ductility was almost the same for all the samples regardless of the annealing temperature. For simplicity, as a first step, the current work focused on the Al/Ti/Al LMCs composed of the fully recrystallized Ti and Al layers, which were annealed at 600 °C for 1 h. It is worth noting that the detailed mechanism for the improved ductility in the Al/Ti/Al LMCs may vary with the degree of recrystallization, which will be evaluated in future work.

3.4. Strain distribution after tension

To explore the underlying mechanism for the improved ductility in the Al/Ti/Al LMCs, the strain distribution and its evolution under tension were investigated via the DIC technique. The DIC technique has been used in many previous research reports (Huang et al., 2018b; Wu et al., 2017) to observe the local strain distribution of layered composites. Based on DIC analyses, it was found that the strain component along the loading direction ($e_{L\text{-}TD}$) was relatively homogeneous in the Ti layer and the Al layer during tension, indicating the principle of iso-strain. However, the strain component along the thickness direction ($e_{T\text{-}ND}$) was obviously inhomogeneous between the Ti layer and Al layer with increasing applied tensile strain, as indicated in Fig. 5. It can be seen in Fig. 5(a) that strain concentration close to the interface occurred from a very small tensile strain (~3%), as marked by the white arrow. With increasing

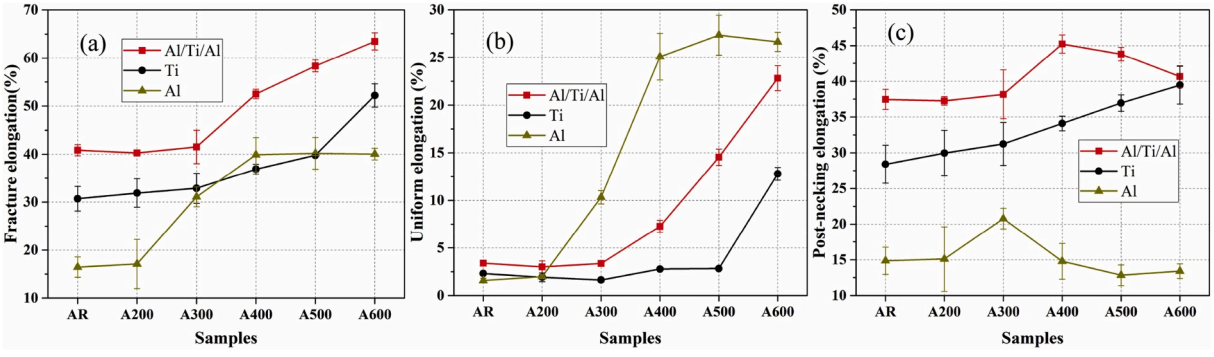

Fig. 3. Tensile elongations of the Al/Ti/Al LMCs, monolithic Ti, and monolithic Al after annealing at various temperatures: (a) fracture elongation, (b) uniform elongation, and (c) post-necking elongation.

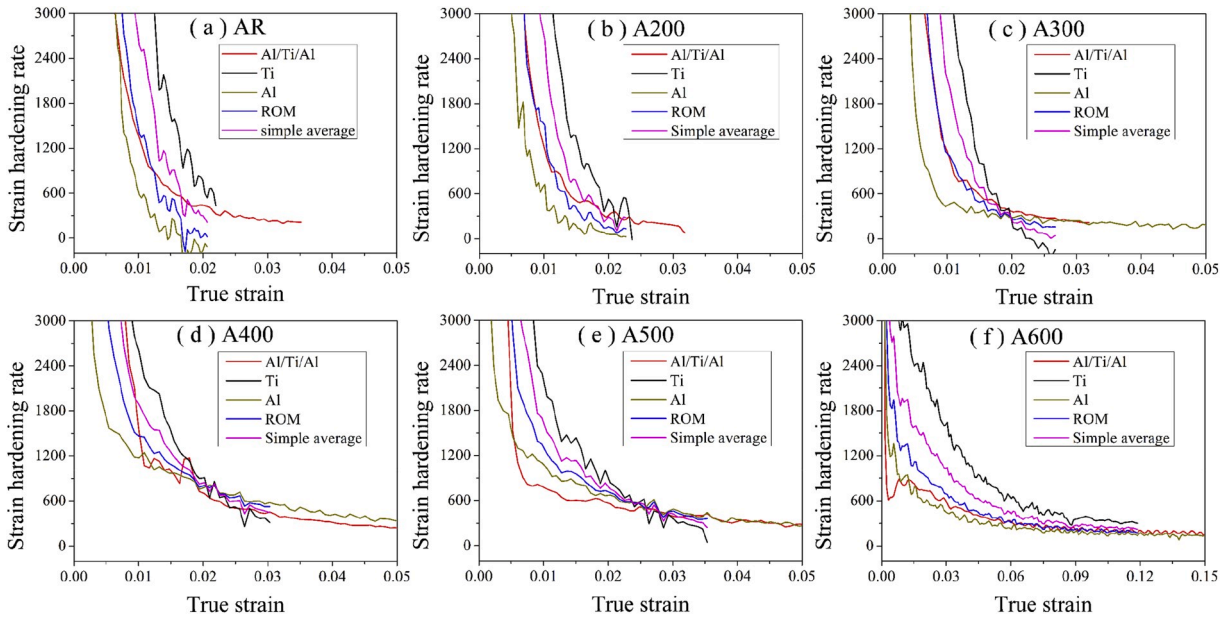

Fig. 4. Experimental and calculated (based on the rule of mixtures (ROM) and the simple average of Ti and Al) strain hardening rate (*d(true stress)/d (true strain)*) as a function of the true strain of the Al/Ti/Al LMCs, monolithic Ti, and monolithic Al after annealing at various temperatures: (a) AR, (b) A200, (c) A300, (d) A400, (e) A500, and (f) A600.

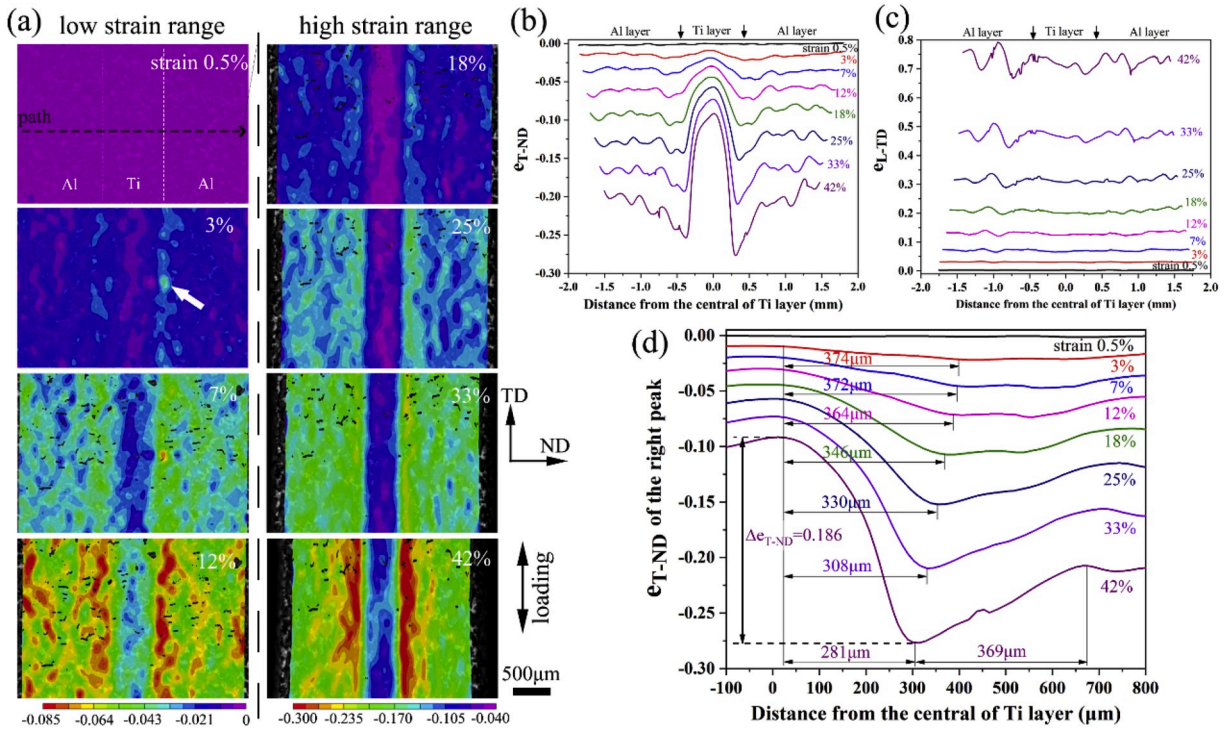

Fig. 5. (a) Strain ($e_{T\text{-}ND}$, along the thickness direction) distribution of Al/Ti/Al LMCs during tension along TD. Dashed white lines mark the initial Ti/Al interface boundary. Strain distribution curves along the specific path shown in (a) at different tensile strain levels: (b) $e_{T\text{-}ND}$, strain component along the thickness direction of the tensile sample (ND of LMCs sheet), (c) $e_{L\text{-}TD}$, strain component along the loading direction of the tensile sample (TD of LMCs sheet), and (d) an enlarged version of the right part of (b).

applied tensile strain, the strain localization ($e_{T\text{-}ND}$) near the interface was remarkably intensified. At the same time, the local strain in the Al layer was higher than that in the Ti layer (thus there was a larger compressive deformation along the thickness direction in the Al layer), and this increased as the applied tensile strain increased. The inhomogeneous local strain distribution between the Ti layer and Al layer should create a strain gradient near the Ti/Al interface.

For quantitative determination of the strain distribution, $e_{T\text{-}ND}$ (along thickness direction) and $e_{L\text{-}TD}$ (along loading direction) along the specific path are presented in Fig. 5(b) and (c). For $e_{T\text{-}ND}$, Fig. 5(b) indicates that an obvious strain gradient exists near the interface. The magnitude of the strain discrepancy between the Ti layer and the Al layer increased with increasing applied tensile strain. The distance from the maximum strain to the minimum strain on the Ti side or Al side, which is temporarily defined as the width of the interface affected zone (IAZ) (Huang et al., 2018a; Ma et al., 2016), decreased as the applied tensile strain increased, as shown in Fig. 5 (d) (which is a magnified version of Fig. 5(b)). The width of the IAZ changed with the applied strain, which is different from a previously reported study on bronze/copper laminated composites (Huang et al., 2018a; Ma et al., 2016). However, because the overall thickness of the Ti layer or Al layer also reduced, the ratio of the width of the IAZ with respect to the overall thickness may not obviously reduce.

It is worth noting that the widths of the IAZ on the Ti side and the Al side were ~281 μm and ~369 μm at an applied strain level of 42%, respectively, which were more than one order of magnitude larger than reported values (~5–6 μm for bronze/copper and ~15 μm for Ti/Al) (Huang et al., 2018a; Huang, 2019; Ma et al., 2016). In the IAZ, the strain displayed a gradient distribution, which is generally assumed to be accommodated by GNDs (Wu and Zhu, 2017). The introduction of a large number of GNDs may contribute to the extra strengthening (Fig. 2) in the current work. However, a higher strain hardening rate that supposed to associate with the

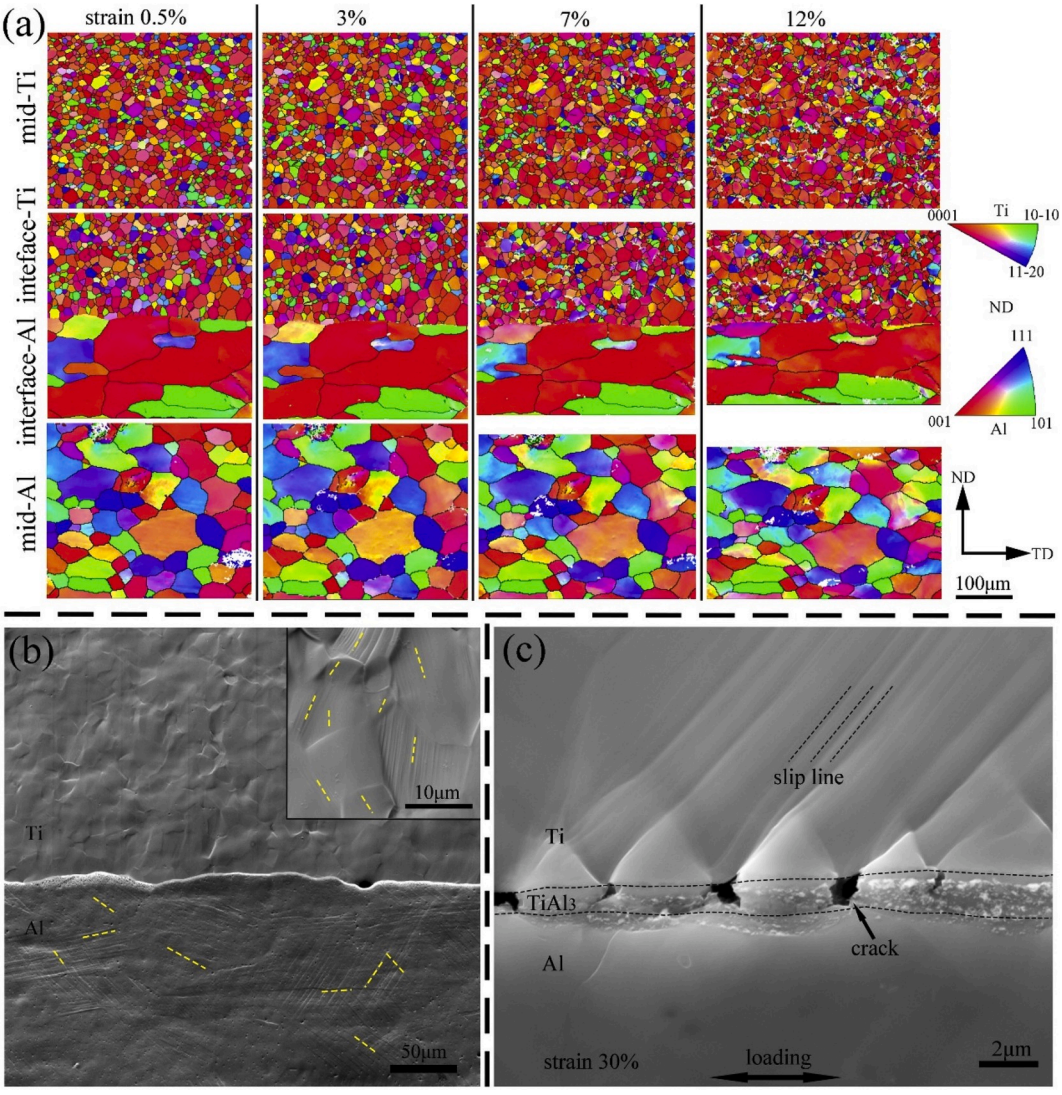

Fig. 6. (a) Ex-situ orientation image maps (IPF maps) of the A600 sample after different strains; (b) typical slip lines near the Ti/Al interface after 3% strain; (c) cracks at the interface of Al/Ti/Al LMCs after 30% strain.

presence of GNDs was not found in the thick Al/Ti/Al LMCs (as shown in Fig. 4) compared with the constituent materials, which contrasts with the results from a previous study (Huang et al., 2018b).

One may note that the through-thickness strain ($e_{T\text{-}ND}$) displayed a negative gradient, i.e. the higher plastic strain the nearer the interface. This is contrary to the strain gradient produced by GNDs pile-ups from Frank–Read sources. Huang et al. (2018a) believed that the ledges on the interface between layers could act as sources to emit dislocations, which was consistent with a view that interfaces such as grain boundaries were the primary dislocation sources (Mompiou et al., 2013). While, based on in-situ observation of dislocation near the interface, Zhou et al. (2019) reported that the strain gradient near interfaces cannot be quantitatively related to the density gradient of GNDs. The strain gradient was assumed primarily produced by Frank–Read source gradient instead of dislocation pile-ups (Zhou et al., 2019). It seems that the controversy on how dislocations interact with interfaces need be further explored.

Nevertheless, the IAZ demonstrates interface coupling, which is also a result of the compatible deformation of the Ti layer and Al layer. The large width of the IAZ plays a crucial role in improving the ductility of the Al/Ti/Al thick LMCs. The cause of the wide IAZ will be further discussed in section 5.1. In contrast, the strain along the loading direction ($e_{L\text{-}TD}$) displays a relatively uniform distribution despite the applied tensile strain, as indicated in Fig. 5(c). The local $e_{L\text{-}TD}$ may be higher than the nominal strain as a result of necking.

3.5. *Deformation mechanism analysis based on ex-situ slip trace*

Non-uniform deformation is generally related to non-uniform stress distribution. Therefore, the stress state in the IAZ may not belong to the uniaxial tensile state anymore. Wu et al. (2014a, 2014b) reported that complex stress may promote a new plastic deformation mechanism that differs from the uniaxial tensile stress; however, no direct evidence was provided for this. In this work,

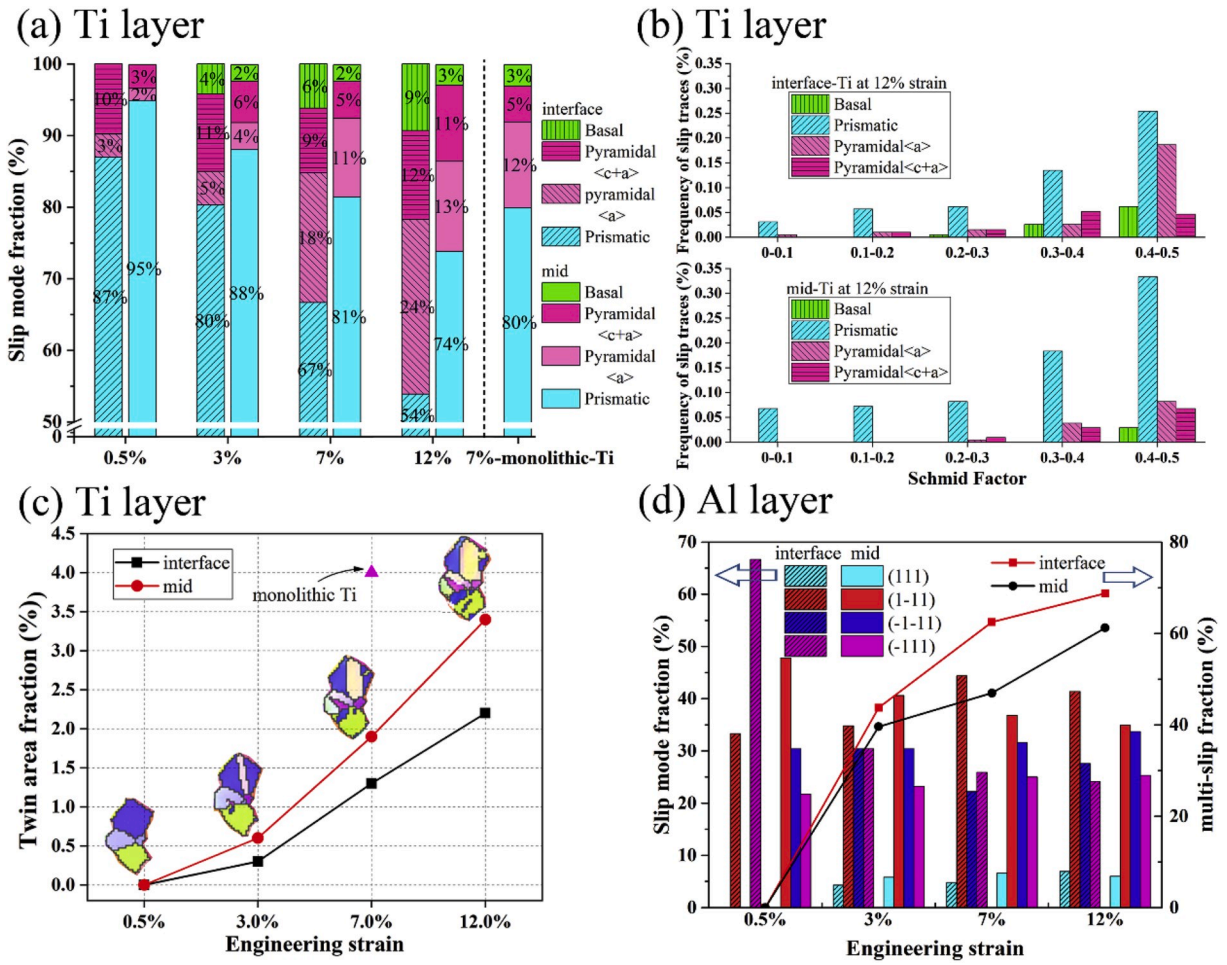

Fig. 7. (a) Statistics of slip activity in the mid-Ti, interface-Ti, and monolithic Ti at different strains (if multiple slip systems are activated in one grain, each type is counted once); (b) SFs of the activated pyramidal slip in the interface-Ti and mid-Ti at a strain of 12%; (c) twin area fraction after different tensile deformations; (d) statistics of the slip system in the interface-Al and mid-Al at different strains and the fraction of grains with multi-slip.

the deformation modes were analyzed based on the slip trace method. Ex-situ microstructure characterization via SEM and EBSD was performed on interruption of the tension for the A600 sample. Four local regions, including the regions close to the interface and the central regions of the Ti layer and the Al layer were observed. For convenience, these four regions are named interface-Ti, interface-Al, mid-Ti, and mid-Al, respectively. Fig. 6(a) shows the inverse pole figure (IPF) maps of the different local regions under various tensile strains. At the same time, slip lines can be observed via SEM, as shown in Fig. 6(b).

Furthermore, micro-cracks can be observed at the Ti/Al interface (Fig. 6(c)), which can be attributed to the brittle intermetallic layer ($TiAl_3$) and the large strain near the interface. Most of these micro-cracks are perpendicular to the loading direction, and their propagation is restrained by the layered structure. Additionally, many slip lines can be found near the crack tips in the Ti layer and are distributed at 45° to the tensile direction. The similar restrained crack phenomenon and slip behavior were also reported in a previous study on Ti–Al laminated composites (Qin et al., 2017). The occurrence of these micro-cracks is believed to relieve the strain and stress localization at the interface, which is beneficial for increasing the ductility of the Ti/Al LMCs (Huang et al., 2016, 2018b).

Slip trace analysis was carried out using an in-house code based on the Euler angles obtained from EBSD data and the corresponding slip lines identified via SEM. For Ti, basal <a> slip, prismatic <a> slip, pyramidal I <a>, and pyramidal I <c+a> slip were considered during the theoretical slip trace calculation (Barkia et al., 2015; Orozco-Caballero et al., 2018). Similarly, {111}<110> was considered as the possible activated slip system for Al. The identification process of the specific slip mode is briefly described in Appendix A1.

Fig. 7(a) shows the statistics of the activated slip systems in the mid-Ti and interface-Ti at various tensile strains. Fig. 7(a) indicates that: (1) prismatic slip is the main slip mode in the mid-Ti and interface-Ti up to 12% deformation; (2) the fractions of the pyramidal slip (including pyramidal <a> and pyramidal <c+a>), as well as the basal slip increase with the tensile strain; (3) for a given tensile strain, the fraction of pyramidal slip was higher than the basal slip, although the former is often reported to have higher critical resolved shear stress (CRSS) than the latter (Wang et al., 2020); (4) for a given tensile strain, the fractions of the pyramidal slip and basal slip in the interface-Ti were always higher than that in the mid-Ti; (5) the activated slip systems in the mid-Ti were very similar to those in monolithic Ti at the same tensile strain (7%).

It is interesting to note that the fractions of the pyramidal slip and basal slip in the interface-Ti were always higher than those in the mid-Ti; this is because these two slip systems are believed to have a much higher CRSS than prismatic slip (Wang et al., 2020) and are not easy to activate. In addition, with respect to the macroscopic loading (uniaxial tension along TD), the Schmid factors (SFs) of the activated slip in the Ti layer after 12% strain were calculated and are presented in Fig. 7(b). The prismatic slip is distributed in a wide range of SFs in both interface-Ti and mid-Ti, and the number of them increases with increasing SFs. The pyramidal slip with SFs below 0.2 and basal slip with SFs below 0.4 are not observed in the mid-Ti, which exhibits a typical "Schmid behavior". However, in the interface-Ti, a small amount of pyramidal and basal slip can be activated with relatively lower SFs, 0–0.2 and 0.2–0.4, respectively. The higher fraction of slip systems with a high CRSS but small SFs in the interface-Ti may be related to the complex stress/strain state of the IAZ. The stress state will be further investigated via finite element simulations in section 4. It is worth noting that the extra activation of slip systems with higher CRSS may contribute to the extra strengthening mentioned in Fig. 2.

Additionally, a few twins appeared in the Ti layer of the Al/Ti/Al LMCs during tension along the TD. The twin area fraction at different strains and local regions were also calculated, as presented in Fig. 7(c). It could be found that: (1) the twin area fractions in the interface-Ti and the mid-Ti increased with tensile strain; (2) for a given tensile strain, the twin area fraction at the interface-Ti was always lower than that in the mid-Ti; (3) the twin area fraction in the Ti layer of the Al/Ti/Al LMCs was lower than that in monolithic Ti at the same tensile strain (7%). Fig. 7(c) indicates that the twinning was suppressed by the layered structure in the Al/Ti/Al LMCs, and the suppressing effect was enhanced closer to the interface. Twinning was also reported to be hindered by the layered structure in a previous study on Ti/Al LMCs (Huang et al., 2016). It was reported that the activation of twins may cause an increase of the strain hardening rate in Ti (Tanaka et al., 2010). Therefore, suppression of twinning in the Ti layer of the Al/Ti/Al LMCs as a result of the layered structure may contribute to the relatively low strain hardening rate of the Al/Ti/Al LMCs in this study (Fig. 4).

The activated slip systems in the interface-Al and mid-Al at various tensile strains were counted. The fractions of the activated slip systems on different slip planes are presented in Fig. 7(d). The statistics indicated that the activated slip systems in the interface-Al were very similar to that in the mid-Al, which differed from those in the Ti layer. This may be attributed to the face-centered cubic crystal structure of Al, which has a higher crystal symmetry than the hexagonal close-packed structure of Ti. However, the fraction of grains with multi-slip in the interface-Al was higher than that in the mid-Al. Grains with multi-slip mean that the slip lines in one grain can be identified to belong to different slip planes. The higher fraction of multi-slip in the interface-Al may also be related to the local complex stress/strain state near the interface.

4. Finite element simulations

To further investigate the deformation behavior of Al/Ti/Al LMCs under tension, finite element (FE) simulations were conducted. As mentioned about Fig. 1(g) and (h), a relatively strong texture was observed in the Ti layer and Al layer, which generally causes obvious anisotropy (Baral et al., 2018; Kuwabara et al., 2017; Yang et al., 2020). Therefore, plastic anisotropy was considered during FE simulations. In this section, the constitutive model and the parameter identification are first introduced; then, the simulation results are presented and validated.

4.1. Anisotropic elastic-plastic constitutive model

To describe the plastic anisotropy and the asymmetric yielding, Plunkett et al. (2008) proposed a yield criterion, which involves two linear transformations and can be expressed as:

$$f_P(\boldsymbol{\Sigma}^{(1)},\boldsymbol{\Sigma}^{(2)}) = \left(\left|\Sigma_1^{(1)}\right| - k_P^{(1)}\Sigma_1^{(1)}\right)^a + \left(\left|\Sigma_2^{(1)}\right| - k_P^{(1)}\Sigma_2^{(1)}\right)^a + \left(\left|\Sigma_3^{(1)}\right| - k_P^{(1)}\Sigma_3^{(1)}\right)^a + \left(\left|\Sigma_1^{(2)}\right| - k_P^{(2)}\Sigma_1^{(2)}\right)^a + \left(\left|\Sigma_2^{(2)}\right| - k_P^{(2)}\Sigma_2^{(2)}\right)^a + \left(\left|\Sigma_3^{(2)}\right| - k_P^{(2)}\Sigma_3^{(2)}\right)^a, \tag{2}$$

where $\Sigma_i^{(1)}$ and $\Sigma_i^{(2)}, i = 1...3$ are the principal values of transformed stress tensors $\boldsymbol{\Sigma}^{(1)}$ and $\boldsymbol{\Sigma}^{(2)}$, in which the superscript indicates the label of transformation; a is the degree of homogeneity; $k_P^{(1)}$ and $k_P^{(2)}$ are material parameters to describe asymmetric yielding, which are assumed to be zero in the current work because the main stress state is the tensile stress state.

The transformed stress tensors are defined as:

$$\boldsymbol{\Sigma}^{(1)} = \mathbf{C}^{(1)} : \mathbf{S} \tag{3}$$

$$\boldsymbol{\Sigma}^{(2)} = \mathbf{C}^{(2)} : \mathbf{S} \tag{4}$$

where $\mathrm{C}^{(1)}$ and $\mathrm{C}^{(2)}$ are fourth-order tensors and $\mathbf{S}$ is the deviatoric part of the Cauchy stress tensor $\boldsymbol{\sigma}$. Let (x_1, x_2, x_3) be a reference frame associated with orthotropy. In the case of a sheet, x_1, x_2 and x_3 are assumed to represent the rolling, transverse, and normal direction, respectively. Relative to the orthotropy axes (x_1, x_2, x_3), the fourth-order tensor $\mathrm{C}^{(1)}$ and $\mathrm{C}^{(2)}$ operating on the stress deviator can be represented by the 6 × 6 matrix:

$$C^{(1)} = \begin{bmatrix} c_{11}^{(1)} & c_{12}^{(1)} & c_{13}^{(1)} & 0 & 0 & 0 \\ c_{12}^{(1)} & c_{22}^{(1)} & c_{23}^{(1)} & 0 & 0 & 0 \\ c_{13}^{(1)} & c_{23}^{(1)} & c_{33}^{(1)} & 0 & 0 & 0 \\ 0 & 0 & 0 & c_{44}^{(1)} & 0 & 0 \\ 0 & 0 & 0 & 0 & c_{55}^{(1)} & 0 \\ 0 & 0 & 0 & 0 & 0 & c_{66}^{(1)} \end{bmatrix},\ C^{(2)} = \begin{bmatrix} c_{11}^{(2)} & c_{12}^{(2)} & c_{13}^{(2)} & 0 & 0 & 0 \\ c_{12}^{(2)} & c_{22}^{(2)} & c_{23}^{(2)} & 0 & 0 & 0 \\ c_{13}^{(2)} & c_{23}^{(2)} & c_{33}^{(2)} & 0 & 0 & 0 \\ 0 & 0 & 0 & c_{44}^{(2)} & 0 & 0 \\ 0 & 0 & 0 & 0 & c_{55}^{(2)} & 0 \\ 0 & 0 & 0 & 0 & 0 & c_{66}^{(2)} \end{bmatrix}.$$

The yield criterion (2) was used here because of its flexibility. The components in the fourth-order tensors $\mathrm{C}^{(1)}$ and $\mathrm{C}^{(2)}$ are referred to as anisotropy parameters, which are to be identified based on experimental data.

Yielding is assumed to be described by:

$$F(\boldsymbol{\sigma},\bar{\varepsilon}_P) = \bar{\sigma}(\boldsymbol{\sigma},\bar{\varepsilon}_P) - Y(\bar{\varepsilon}_P), \tag{5}$$

where $\bar{\sigma}(\boldsymbol{\sigma},\bar{\varepsilon}_P)$ is the effective stress based on potential given by Equation (6):

$$\bar{\sigma}(\boldsymbol{\sigma},\bar{\varepsilon}_P) = A\left[f_P(\boldsymbol{\Sigma}^{(1)},\boldsymbol{\Sigma}^{(2)})\right]^{1/a}. \tag{6}$$

In Equation (6), A is a constant defined such that $\bar{\sigma}$ reduces to the tensile yield stress in the rolling direction. In Equation (5), $Y(\bar{\varepsilon}_P)$ is the isotropic hardening model in which $\bar{\varepsilon}_P$ is the effective plastic strain. The effective plastic strain associated with the anisotropic yield function (5) is calculated using the principle of equivalence of plastic work. Equation (7) describes the isotropic hardening, which is expressed as:

$$Y(\bar{\varepsilon}_P) = \sigma_0 + Q_1(1 - \exp(-b_1\bar{\varepsilon}_P)) + Q_2(1 - \exp(-b_2\bar{\varepsilon}_P)), \tag{7}$$

where σ_0 is the initial yielding stress and Q_1, Q_2, b_1, and b_2 are material parameters.

It is worth noting that the anisotropy parameters in the fourth-order tensors $\mathrm{C}^{(1)}$ and $\mathrm{C}^{(2)}$ evolve with the effective plastic strain $\bar{\varepsilon}_P$ because of texture evolution. Therefore, to consider the evolution of the anisotropy with increasing strain, the approach proposed by Plunkett et al. (2006) was used. For a finite set of values of effective plastic strain, say $\bar{\varepsilon}_P^1 < \bar{\varepsilon}_P^2 < \cdots < \bar{\varepsilon}_P^M$, the parameter a and components of the fourth-order tensors $\mathrm{C}^{(1)}$ and $\mathrm{C}^{(2)}$ can be determined based on the available experimental data. Then, the effective stress $\bar{\sigma}^j$ and $Y(\bar{\varepsilon}_P^j)$ can be calculated, corresponding to each of the individual strain levels $\bar{\varepsilon}_P^j$, $j = 1, ...M$. Furthermore, a linear interpolation procedure was used to obtain the yield surface corresponding to any given level of accumulated strain. For a given arbitrary strain $\bar{\varepsilon}_P$ ($\bar{\varepsilon}_P^j \le \bar{\varepsilon}_P \le \bar{\varepsilon}_P^{j+1}, j = 1, ...M-1$), the anisotropic yield function is of the form:

$$F(\boldsymbol{\sigma},\bar{\varepsilon}_P) = \Gamma(\boldsymbol{\sigma},\bar{\varepsilon}_P) - \Pi(\bar{\varepsilon}_P), \tag{8}$$

with

$$\Gamma(\boldsymbol{\sigma},\bar{\varepsilon}_P) = w(\bar{\varepsilon}_P)\cdot\bar{\sigma}^j + (1 - w(\bar{\varepsilon}_P))\cdot\bar{\sigma}^{j+1}, \tag{9}$$

and

$$\Pi(\bar{\varepsilon}_P) = w(\bar{\varepsilon}_P)\cdot Y(\bar{\varepsilon}_P^j) + (1 - w(\bar{\varepsilon}_P))\cdot Y(\bar{\varepsilon}_P^{j+1}). \tag{10}$$

The weighting parameter $w(\bar{\varepsilon}_P)$ appearing in Equations (9) and (10) is defined as:

$$w(\bar{\varepsilon}_P) = \frac{\bar{\varepsilon}_P^{j+1} - \bar{\varepsilon}_P}{\bar{\varepsilon}_P^{j+1} - \bar{\varepsilon}_P^{j}}. \tag{11}$$

The yielding function (8) and the isotropic hardening model (7) were implemented in the commercial FEM code ABAQUS/Explicit as user defined materials by VUMAT. The integration algorithm is briefly described in Appendix A2.

4.2. Parameter identification

To identify the parameters in the anisotropic yield function and the isotropic hardening model, uniaxial tension along 0°, 22.5°, 45°, 67.5°, and 90° with respect to the RD were carried out for monolithic Ti and monolithic Al annealed at 600 °C. The measured true stress-true strain curves are presented in Fig. 8(a) and (b). In addition, the Lankford coefficients (r-value) along different directions were also calculated as:

$$r = \frac{\varepsilon_w}{\varepsilon_t} \tag{12}$$

where ε_w and ε_t are the true strains in the width and thickness direction of the tension sample, respectively. The average r-values are shown in Fig. 8(c). Obvious anisotropy existed for the flow stress and r-value, especially for Ti.

For a set of strain levels, say 0.002, 0.012, 0.022, …0.252, the flow stresses and r-values along different directions were used to identify the anisotropy parameters in the yield criterion (2). The highest strain level 0.252 was selected because it was close to the maximum uniform tensile deformation for Al. Although the highest strain level was higher than the maximum uniform tensile

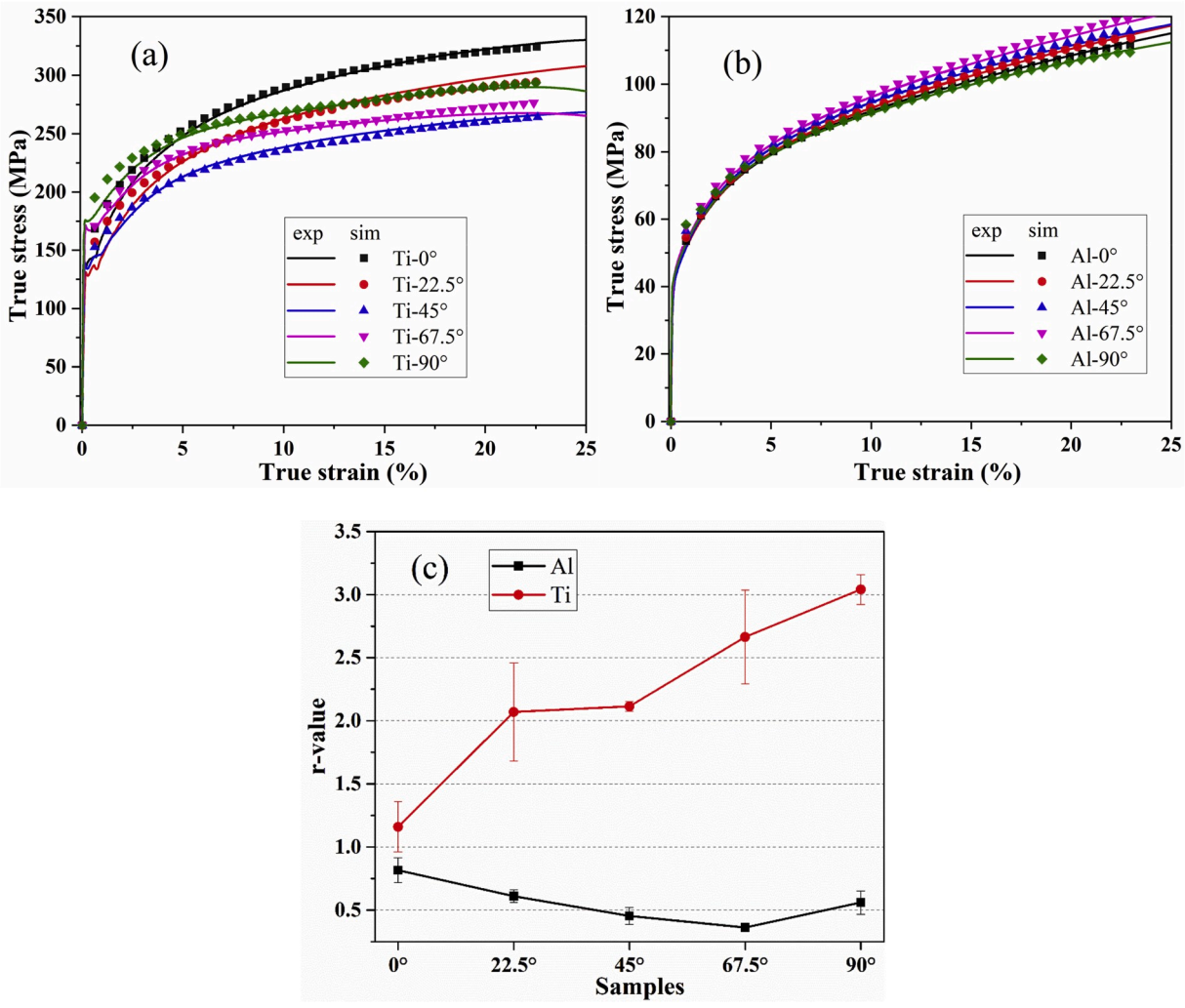

Fig. 8. Comparison between the experimental and simulated true stress-true strain curves of (a) Ti and (b) Al tension along 0°, 22.5°, 45°, 67.5°, and 90° with respect to the RD and (c) r-values.

deformation for Ti, the nominal true flow stress was used without modification in the current work because of the light necking of Ti. The anisotropy parameters were calculated by minimizing the error function (see Appendix A3 for more details), which is defined as:

$$E\left(C^{(1)}, C^{(2)}\right) = \sum_{n=1}^{N} w_n \left(\frac{\sigma_n^{pr}}{\sigma_n^{\exp}} - 1\right)^2 + \sum_{k=1}^{K} w_k \left(\frac{r_k^{pr}}{r_k^{\exp}} - 1\right)^2, \tag{13}$$

where n represents the number of experimental flow stresses (σ) and k represents the number of experimental r-values (r) available. w_n and w_k are the weight coefficients. In the error function, the superscript denotes whether the value is experimental (*exp*) or predicted (*pr*).

The isotropic hardening parameters in (7) can be determined by fitting the true stress-strain curves along the RD. The isotropic hardening parameters and the initial anisotropy parameter (corresponding to a strain level 0.002) values for the monolithic Ti and monolithic Al are shown in Table 1 and Table 2. Based on the identified parameters and the evolution approach, the simulated true stress-true strain curves (sim) were compared with the experimental results (exp), as shown in Fig. 8(a) and (b). The simulated curves agreed well with the experimental results, indicating good parameter identification.

4.3. Simulation results on the tension of Al/Ti/Al LMCs

The same geometry information used for the experimental tension of Al/Ti/Al LMCs, including the gauge area and layer thickness, was used to build the FE model. For simplicity, the gripping part of the tension sample was ignored and a 1/8 model was built. The C3D8R element was used in the current FE simulation. The mesh size near the Ti/Al interface was refined to capture potential strain localization. For comparison, all the layers were assigned as Ti in some simulation cases, which was used to model the tension of monolithic Ti.

Fig. 9 compares the simulated and the experimental results of the Al/Ti/Al LMCs after tension (25%). Fig. 9(a) shows the cross-section profile obtained from the experiment, which indicates that the rectangular cross-section takes an "H"-like shape after tension. The simulated cross-section profile (Fig. 9(c)) also exhibited an "H"-like shape and was basically consistent with the experimental profile (shown by the black dotted line in Fig. 9(c)). To further verify the reliability of the simulation results, the stress-strain curves from the simulation and experiment are compared in Fig. 9(b). It was found that the simulated flow stress was always lower than the experimental result. However, the simulated stress-strain curve was very close to that calculated using the ROM. This is reasonable because the extra strengthening effects by the accumulation of GNDs and the extra activation of pyramidal slip and basal slip were not considered in the current FE model.

The "H"-like deformed cross-section may be attributed to the r-value (ratio between the width strain to the thickness strain). In the presence of tension along the TD, Fig. 8(c) indicated that the average r-value for Ti was ~3.1, while the average r-value for Al was ~0.5. With a high r-value (>1), the Ti layer tended to show a much higher contraction along the width (RD of LMCs) than along the thickness direction (ND of LMCs). In contrast, with a small r-value (<1), the Al layer tended to show less contraction along the width, but more contraction along the thickness direction. This is the reason for $e_{T\text{-}ND}$ in the Al layer being larger than in the Ti layer (Fig. 9(c)) and the strain along the width direction ($e_{w\text{-}RD}$) in the Al layer being less than in the Ti layer (Fig. 9(d)). Compared with the Al layer, the higher contraction deformation along the width direction in the Ti layer caused the "H"-like cross-section. Because the r-values indicating plastic anisotropy were considered in the FE simulations, the main characteristic of inhomogeneous deformation of Al/Ti/Al LMCs under tension was well captured.

The simulated strain distributions along the central path of the tensile sample for the Al/Ti/Al LMCs and monolithic Ti are presented in Fig. 10. For Al/Ti/Al LMCs, the strain component along the thickness direction ($e_{T\text{-}ND}$) shows significant inhomogeneous distribution between the Ti layer and the Al layer with increasing applied tensile strain (Fig. 10(a)). A strain gradient exists between the Ti layer and the Al layer. The amplitude of the strain discrepancy between the Ti layer and the Al layer increased with increasing applied tensile strain. There was a concentration of strain near the Ti/Al interface. These trends are near those determined from the DIC results (the dotted curve in Fig. 10(a) as well as curves in Fig. 5), which demonstrates the reliability of the following analysis based on this model.

It should be noted that the strongest strain concentration was in the Al layer rather than at the exact Ti/Al interface, which may be related to the requirement for stress balance between the Ti layer and the Al layer. It is hard to identify the location of the exact interface from the DIC investigation in the current work (Fig. 5). Hence, whether or not the highest strain concentration is located at the exact Ti/Al interface needs to be studied further in future work. Because the strongest strain concentration was not located at the exact Ti/Al interface, the distance from the maximum strain location to the Ti/Al interface was smaller than the distance (width of IAZ

Table 1
Isotropic hardening parameter and initial anisotropy parameter values for Ti.

$c_{11}^{(1)}$	$c_{12}^{(1)}$	$c_{13}^{(1)}$	$c_{22}^{(1)}$	$c_{23}^{(1)}$	$c_{33}^{(1)}$	$c_{44}^{(1)}$	$c_{55}^{(1)}$	$c_{66}^{(1)}$
0.6578	0.3280	0.4270	0.6759	−0.2696	0.6471	0.9917	1.0000	1.0000
$c_{11}^{(2)}$	$c_{12}^{(2)}$	$c_{13}^{(2)}$	$c_{22}^{(2)}$	$c_{23}^{(2)}$	$c_{33}^{(2)}$	$c_{44}^{(2)}$	$c_{55}^{(2)}$	$c_{66}^{(2)}$
−0.0877	−0.3320	0.1324	0.8635	0.3201	1.0878	1.1849	1.0000	1.0000
$k_P^{(1)}$	$k_P^{(2)}$	b_1	Q_1	b_2	Q_2			
0.0000	0.0000	71.35	50.74	11.21	137.56			

Table 2
Isotropic hardening parameter and initial anisotropy parameter values for Al.

$c_{11}^{(1)}$	$c_{12}^{(1)}$	$c_{13}^{(1)}$	$c_{22}^{(1)}$	$c_{23}^{(1)}$	$c_{33}^{(1)}$	$c_{44}^{(1)}$	$c_{55}^{(1)}$	$c_{66}^{(1)}$
0.4541	0.1141	−0.6675	1.0284	−0.0774	0.5273	0.8008	1.0000	1.0000
$c_{11}^{(2)}$	$c_{12}^{(2)}$	$c_{13}^{(2)}$	$c_{22}^{(2)}$	$c_{23}^{(2)}$	$c_{33}^{(2)}$	$c_{44}^{(2)}$	$c_{55}^{(2)}$	$c_{66}^{(2)}$
1.0701	−0.1780	0.0799	0.3635	−0.7054	0.4369	1.0156	1.0000	1.0000
$k_P^{(1)}$	$k_P^{(2)}$	b_1	Q_1	b_2	Q_2			
0.0000	0.0000	53.63	24.91	3.68	76.41			

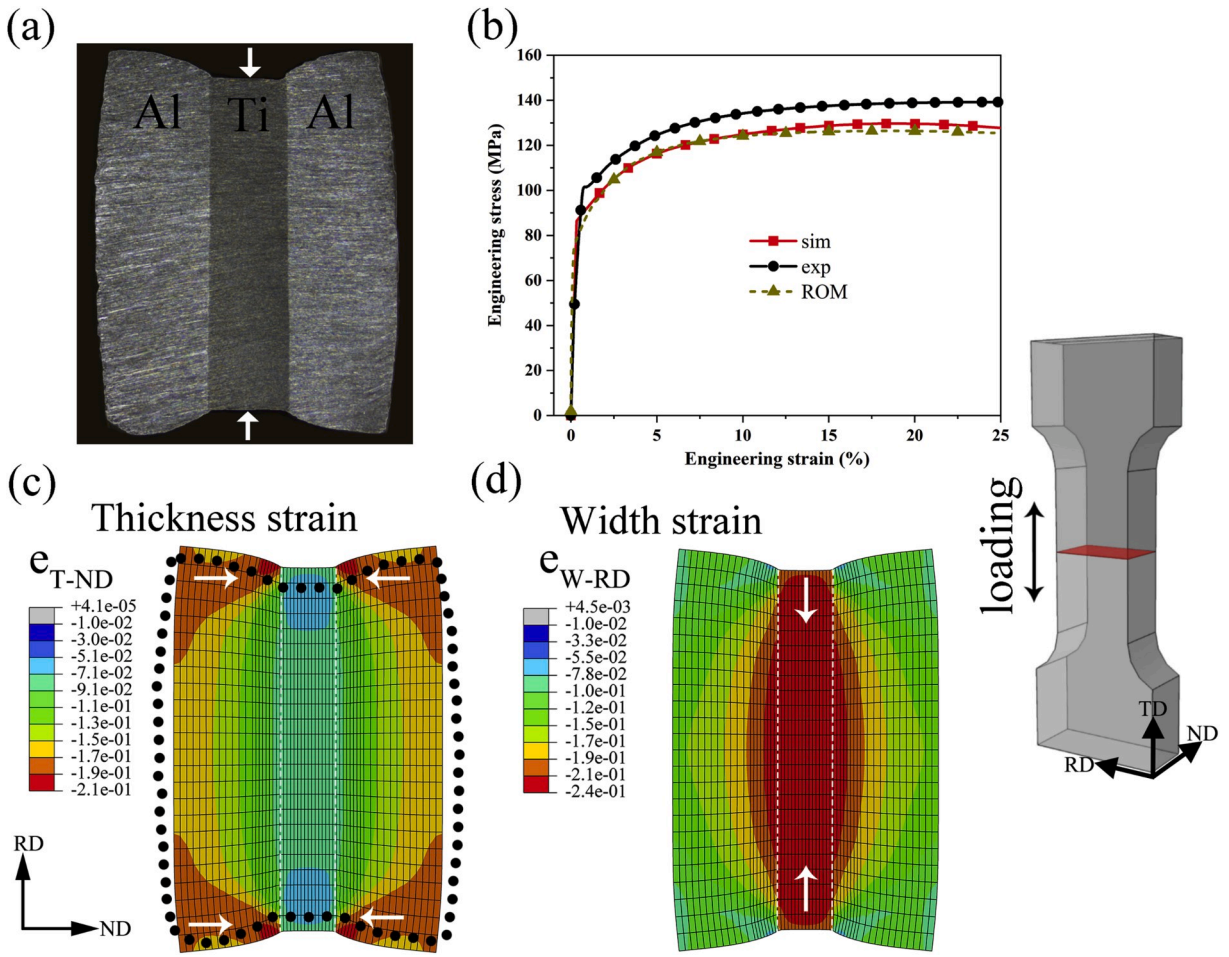

Fig. 9. Comparison between the simulated and experimental results of Al/Ti/Al LMCs after 25% tension along the TD: (a) experimental profile of the cross-section observed via optical microscopy, (b) comparison between the simulated and the experimental engineering stress-strain curves, (c) comparison between the simulated and the experimental cross profiles (the black dotted line), and (d) distribution of $e_{w\text{-}RD}$ on the cross-section.

in the current work) from the maximum strain to the minimum strain location. For example, when the applied tensile strain was 25%, the simulated distance from the maximum strain to the Ti/Al interface was ~167 μm, while the simulated width of the IAZ was ~276 μm, as shown in Fig. 10(a). The simulated width of the IAZ decreased with increasing applied strain, which agreed well with the trend from the DIC tests. In addition, compared with $e_{T\text{-}ND}$, the strain component along the tensile direction ($e_{L\text{-}TD}$) showed an almost homogeneous distribution (Fig. 10(b)) between the Ti layer and Al layer. The simulated strains on the TD-ND plane of Al/Ti/Al LMCs showed a similar distribution trend as the DIC experimental results (Fig. 5), which validated the simulations.

However, the simulated widths (Fig. 10(a)) of the IAZ were smaller than the DIC results (Fig. 5(d)). The simulated strain values were also different from the values obtained from the DIC results. These discrepancies between the simulated results and the experimental results may be caused by the use of a phenomenological elastic-plastic constitutive model; a lot of deformation mechanisms are not considered in such a model, e.g., the extra activation of pyramidal slip in the interface-Ti and GNDs accumulation. For comparison, all strain components on the TD-ND plane of monolithic Ti showed a uniform distribution despite the applied tensile strain, as

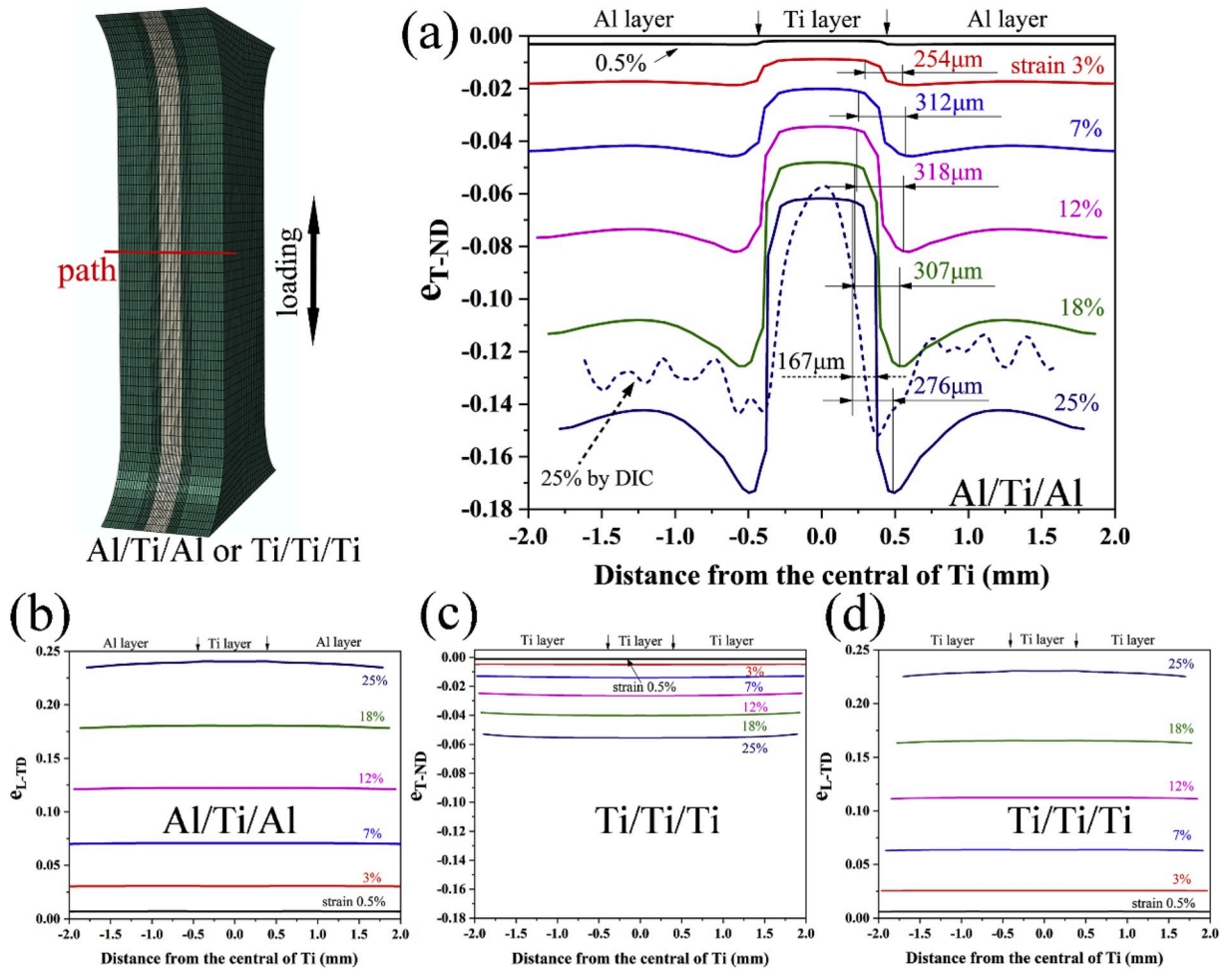

Fig. 10. Simulated strain distribution along the thickness path of the tensile sample after tension along the TD: (a) strain ($e_{T\text{-}ND}$) along the thickness direction of the tensile sample (ND of LMCs) and (b) strain ($e_{L\text{-}TD}$) along the loading direction of the tensile sample (TD of LMCs) of Al/Ti/Al LMCs; (c) strain ($e_{T\text{-}ND}$) along the thickness direction of the tensile sample (ND of sheet); and (d) strain ($e_{L\text{-}TD}$) along the loading direction of the tensile sample (TD of sheet) of Ti/Ti/Ti.

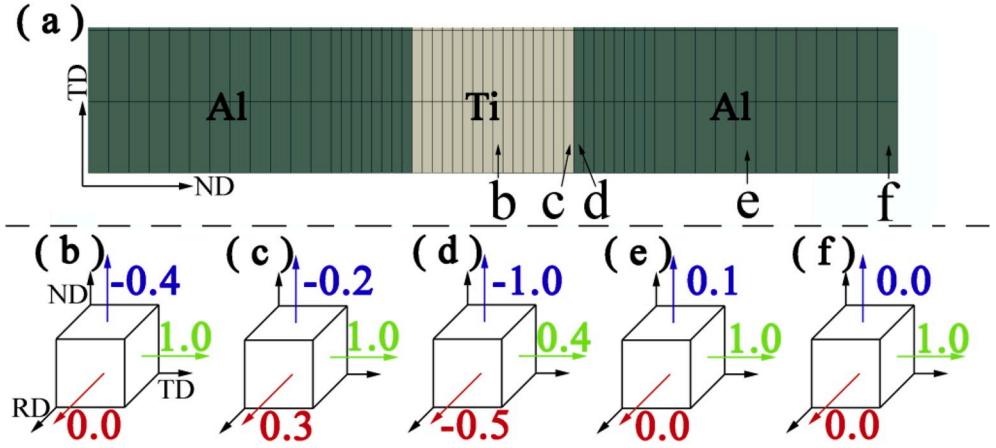

Fig. 11. Simulated normal stress (normalized by the maximum absolute value of stress component) at different local regions in Al/Ti/Al LMCs after 12% tension along the TD: (a) locations of local regions, (b) mid-Ti, (c) interface-Ti, (d) interface-Al, (e) mid-Al, and (f) surface-Al.

indicated by Fig. 10(c) and (d).

Typical simulated stress components at different local regions (mid-Ti, interface-Ti, interface-Al, mid-Al, and the surface of Al) for the Al/Ti/Al LMCs after tension (12%) are shown in Fig. 11. Stress components are normalized by the maximum absolute value of the stress component in each local region. An inhomogeneous stress state could be found along the thickness of the Al/Ti/Al LMCs. In the mid-Ti and mid-Al the stress was two-dimensional. In the local region near the Ti/Al interface, the stress was three-dimensional, which was far from the applied uniaxial tensile stress. On the surface side of the Al layer, the stress could be attributed to the theoretical uniaxial tensile stress along the TD. The FE simulations indicated that compatible deformation between the Ti layer and Al layer changed the applied stress state, which may contribute to the extra activation of pyramidal and basal slip in the interface-Ti. In addition, the complex stress state near the interface may also cause strengthening. This was demonstrated by the simulated flow stress, which was a little higher than the calculated stress based on the ROM, particularly at relatively large strain levels (>13%), as shown in Fig. 9(b).

By considering the anisotropy of Ti and Al, the main character of the inter-layer inhomogeneous deformation behavior of the Al/Ti/Al LMCs during tension can be well captured via FE simulations. However, this does not attempt to develop an accurate constitutive model that can represent all deformation behaviors in the Al/Ti/Al LMCs. As mentioned above, the accumulation of GNDs because of the strain gradient between the Ti layer and the Al layer, the extra activation of pyramidal and basal slips, the suppression of twinning, and the strain rate effect were not accounted for. In principle, the FE simulations in this work were intended to demonstrate the effects of plastic anisotropy of the constituent layer on the local deformation of the Al/Ti/Al LMCs and the formation of the IAZ, which have not been adequately addressed in previous work on layered materials. This work would help in understanding the mechanism of the

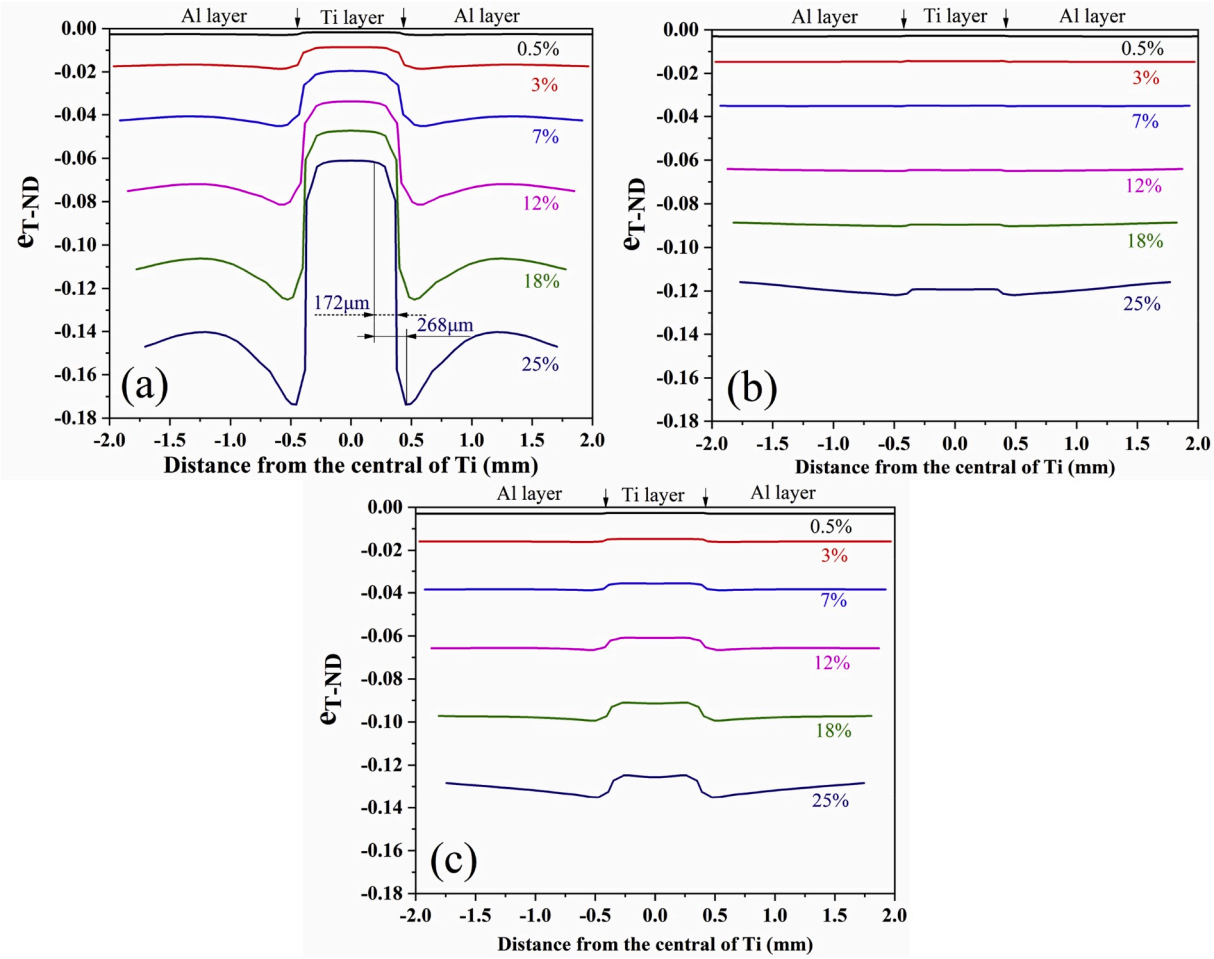

Fig. 12. Simulated strain ($e_{T\text{-}ND}$) distribution in the Al/Ti/Al LMCs after tension under different conditions: (a) identical ultimate elastic strain for the Ti layer and the Al layer with tension along the TD, (b) identical unit r-value in the Ti layer and the Al layer with tension along the TD, (c) tension along the RD.

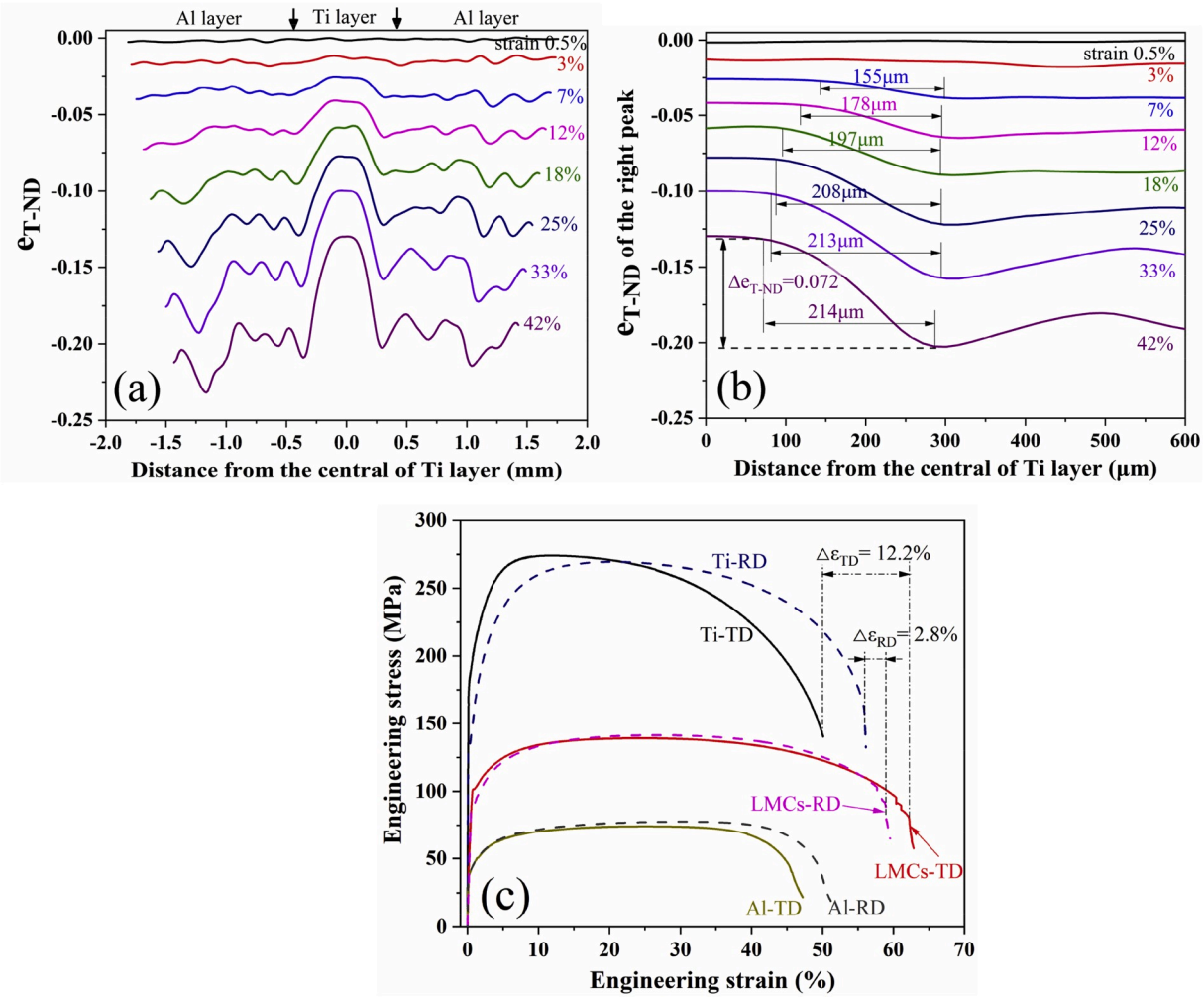

Fig. 13. (a) Experimental strain ($e_{T\text{-}ND}$) distribution along the thickness direction of Al/Ti/Al LMCs after application of different tensions along the RD, (b) an enlarged version of the right part of (a), and (c) comparison of the engineering stress-strain curves of Al/Ti/Al LMCs, monolithic Ti, and monolithic Al for tension along the RD and TD.

extraordinarily high tensile ductility of the Al/Ti/Al thick LMCs. The modeling accuracy for the deformation behavior of the Al/Ti/Al LMCs can be further improved by taking into account the activation of slip and twinning, for example by using a physically-based crystal plasticity constitutive model (Lu et al., 2020; Zhao et al., 2020). Moreover, the effects of GNDs on the deformation behavior of Al/Ti/Al LMCs may be captured by the strain gradient crystal plasticity that established through discussion of the possible higher-order boundary conditions (Bardella, 2006; Gurtin and Needleman, 2005; Kuroda and Tvergaard, 2008).

5. Discussion

5.1. Effect of out-of plane anisotropy of Ti and Al on the IAZ width

The heterogeneity of the strength, plasticity, crystal structure, and grain size between Ti and Al make their deformation highly heterogeneous, which leads to a strain gradient (i.e., IAZ) near the interface (Huang et al., 2018a; Liang et al., 2019; Ma et al., 2016). The reported width of the IAZ was only ~5–6 μm in copper/bronze laminates (Huang et al., 2018a) and ~15 μm in Ti/Al laminates (Huang, 2019). However, in this study, the width of the IAZ for the Al/Ti/Al LMCs could exceed 150 μm, as indicated by the DIC results (Fig. 5(d)) as well as by FEM (Fig. 10(a)). The large width of the IAZ may play a crucial role in improving the fracture elongation for thick Al/Ti/Al LMCs. Understanding the main factors that cause such a large IAZ width may help in the fabrication of a layered material with high strength and high ductility.

Some of the factors affecting the width of the IAZ in thick Al/Ti/Al LMCs have been investigated. Previous studies (Huang et al., 2018b; Kim et al., 2018) believed that the difference in the ultimate elastic strain between the constituent layers played an important role in the formation of the IAZ. Because of the different elastic modulus or/and yield stress between the constituent layers, plastic deformation occurs in some layers, while some layers deform elastically; this causes highly heterogeneous deformation between the constituent layers, leading to the formation of the IAZ (Huang et al., 2018b; Kim et al., 2018). Here, to check the effect of the ultimate elastic strain on the width of the IAZ, the elastic modulus of the Al layer was artificially altered in the FE simulations to obtain the same ultimate elastic strain between the Al layer and Ti layer. Under these conditions, the simulated $e_{T\text{-}ND}$ along the thickness path after tension along TD is shown in Fig. 12(a). The results indicate that the strain distribution was very close to that in the original Al/Ti/Al LMCs (Fig. 10(a)), which implied that a discrepancy in the ultimate elastic strain between the Ti layer and the Al layer had little impact on the width of the IAZ. This may be attributed to the elastic-plastic stage that occurred early in the process for a short period compared with the large plastic deformation (~60%) in Al/Ti/Al LMCs, which results in only a small effect on the IAZ.

The formation of the "H"-like cross-section of the Al/Ti/Al LMCs was attributed to the difference in r-values between the Ti and Al layers. To investigate the effect of the r-value on the IAZ width, the r-values for both the Ti layer and Al layer were artificially changed to 1 in the FE simulations. Under these conditions, the simulated $e_{T\text{-}ND}$ along the thickness path after tension along TD is shown in Fig. 12(b). The results indicate that the strain discrepancy between the Ti layer and the Al layer, the strain concentration, and the width of the IAZ remarkably decreased compared with the original Al/Ti/Al LMCs. This suggested that the difference in the r-value between the Ti layer and the Al layer played a crucial role in realizing a large IAZ width, which contributed to the improved ductility of the thick Al/Ti/Al LMCs.

The r-value discrepancy between the Ti layer and the Al layer is smaller when loading along the RD (r-value_{Ti} - r-value_{Al} = ~0.34)

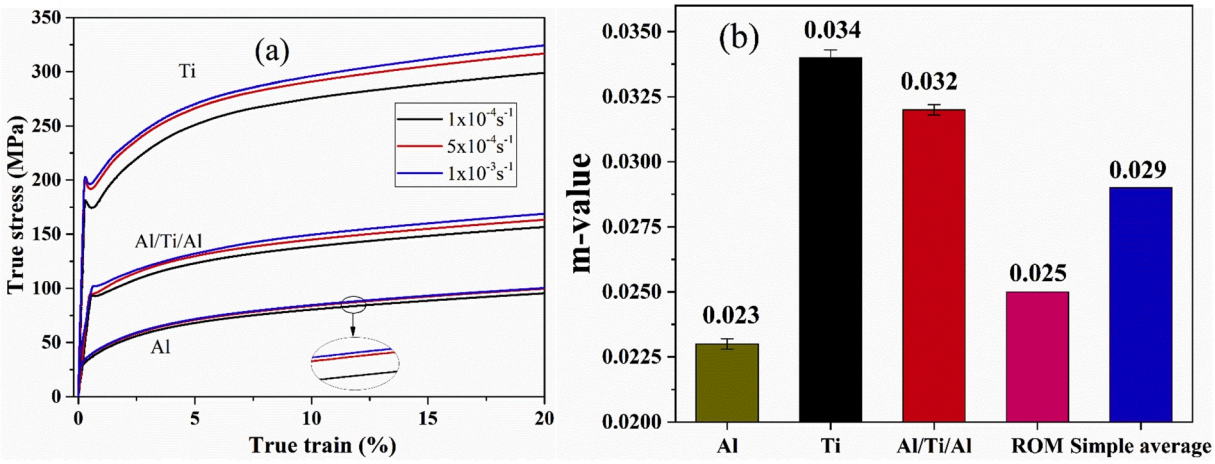

Fig. 14. (a) True stress-strain curves of the Al/Ti/Al LMCs, monolithic Ti, and monolithic Al during tension with different strain rates and (b) tested and calculated (based on the rule of mixture (ROM) and the simple average of Al and Ti) strain-rate sensitivity exponents (m-value).

compared with TD (r-value$_{Ti}$ - r-value$_{Al}$ = ~2.48). If the r-value is an important factor for controlling the width of the IAZ, it can be speculated that the IAZ width for tension along the RD should be smaller than for along the TD. Therefore, tension simulations along the RD were carried out. The simulated $e_{T\text{-}ND}$ is presented in Fig. 12(c). As expected, Fig. 12(c) indicated that for the case of a small r-value difference, the difference in strain between the Ti layer and the Al layer, the strain concentration, and the width of the IAZ are very small compared with the original Al/Ti/Al LMCs. This further indicated that the discrepancy in the r-value between the Ti layer and the Al layer played a crucial role in obtaining a wide IAZ.

The above simulation results indicated that the difference in the r-value between the Ti layer and Al layer is a crucial factor affecting the width of the IAZ. To further confirm this, experiments with tension along the RD were also performed for the Al/Ti/Al LMCs. The distribution and evolution of the $e_{T\text{-}ND}$ for tension along the RD are presented in Fig. 13(a) and (b). The width of the IAZ increased with increasing applied strain, which differs from the results for tension along the TD and may be related to the change in texture. However, the increase in the width of the IAZ reduced as the applied deformation strain increased. When the applied tensile strain was 42%, the width of the IAZ along the RD (~214 μm, Fig. 13(b)) was significantly smaller than for tension along the TD (~281 μm, Fig. 5(d)). In addition, the strain discrepancy ($\Delta e_{T\text{-}ND}$ = 0.072) from the maximum to the minimum point with tension along RD was significantly lower than that for tension along the TD ($\Delta e_{T\text{-}ND}$ = 0.186). These results were in good agreement with the simulated results (Fig. 12) and validate the importance of the r-value for the width of IAZ.

The width of the IAZ is believed to play an important role for optimizing the layer thickness in layered materials. It has been reported that the ductility of layered materials is best when the layer thickness is twice the width of the IAZ (Huang et al., 2018a). In this study, the ratio of the IAZ with respect to the entire Ti layer was ~0.42 (tension along the TD), which means that the thickness of the Ti layer was more than twice the width of the IAZ, even for tension along TD. It was expected that the ductility of the Al/Ti/Al LMCs would deteriorate if the width of the IAZ decreased; to investigate this, the engineering stress-strain curves with tension along the RD and TD were compared, as shown in Fig. 13(c). The ductility (fracture elongation) of the Al/Ti/Al LMCs along the RD was lower than that along the TD. The difference between the fracture elongation along the RD and TD is small (~3%) and one may argue that it was caused by accidental experimental factors. However, it should be noted that the ductility of the monolithic Ti and the monolithic Al were higher for tension along the RD than for the TD, as indicated in Fig. 13(c). Because of the better ductility of the constituent layers, the Al/Ti/Al LMCs would also be expected to have better ductility along the RD, which contradicts the lower observed ductility. On comparing the difference between the fracture elongation of the Al/Ti/Al LMCs and the monolithic Ti (extra ductility), it can be observed that the ductility of the Al/Ti/Al LMCs decreases as the width of the IAZ decreases.

As discussed above, a larger difference between the r-value of the Ti layer and Al layer can cause a larger IAZ width, which leads to a higher ductility for the Al/Ti/Al LMCs. The r-value of Ti and Al can be tailored by changing their texture and has been well studied (Ghosh et al., 2015; Li et al., 2018; Singh and Schwarzer, 2000). This may provide a new strategy to design layered material with a high strength and ductility. However, this viewpoint needs further validation in many other layered materials.

5.2. *Effect of strain-rate sensitivity on the ductility*

The extra ductility (fracture elongation) of the Al/Ti/Al thick LMCs was not caused by strain hardening rate, as mentioned in

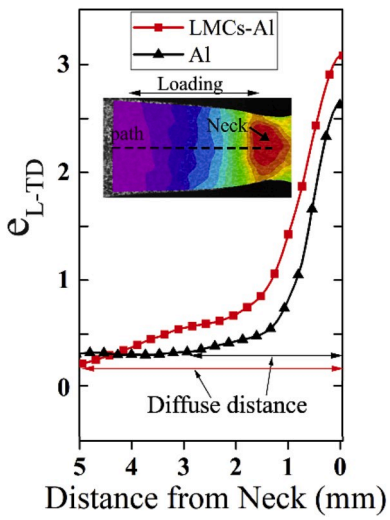

Fig. 15. Strain distribution comparison between the Al/Ti/Al LMCs and monolithic Al after tension along the TD.

section 3.3. In addition, the post-necking elongation of the Al/Ti/Al LMCs was higher than for both the monolithic Ti and monolithic Al. High post-necking elongation has often been attributed to a high strain-rate sensitivity (SRS) (Ghosh, 1977; Jin and Lee, 2012; Li and Ghosh, 2003). Previous studies have also reported that the excellent ductility of Cu/Ni (Fu et al., 2018) can be attributed to the enhanced strain-rate sensitivity. To verify the effect of SRS on the ductility of Al/Ti/Al LMCs, the exponent (m-value) of the SRS was determined via tensile tests. Tension was applied with different strain rates ($\dot{e} = 1 \times 10^{-4}$, 5×10^{-4}, and 1×10^{-3} s^{-1}) for the Al/Ti/Al LMCs, monolithic Ti, and monolithic Al along the TD. The SRS exponent (m-value) was determined by Li et al. (2019b):

$$m = \left.\frac{\partial \ln \sigma}{\partial \ln \dot{e}}\right|_{constant\ strain}. \tag{14}$$

The true stress-strain curves with different strain rates are shown in Fig. 14(a). The results indicated that higher flow stresses were required for tension with higher strain rates, indicating positive m-values. The average m-value for the Al/Ti/Al LMCs, monolithic Ti, and monolithic Al were 0.032 ± 0.0002, 0.034 ± 0.0003, and 0.023 ± 0.0002, respectively. The m-value of the Al/Ti/Al LMCs was very close to that of the monolithic Ti, which was significantly higher than the m-value of monolithic Al.

For monolithic Ti (A600 sample), the uniform elongation was only ~12%, which meant that necking began very early. However, the fracture elongation could reach ~52%. The post-necking elongation accounted for a large fraction (~77%) of the total elongation. In contrast, the post-necking elongation for the monolithic Al (A600 sample) only accounted for ~33% of the total elongation. The much higher post-necking elongation in monolithic Ti may be attributed to its high m-value. Before necking, the strain rate was almost homogeneous across the gauge area. A high SRS would not affect the deformation behavior of Ti. After the onset of necking, strain begins to concentrate near the necking area, which would increase the strain rate in this region. With a high positive m-value, a higher flow stress is required for further deformation when loading with a higher strain rate. This can compensate for the loss of the bearing capability of the material caused by the decrease of the cross area (necking); thus delaying serious strain localization (serious necking) and realizing large post-necking elongation.

For the Al/Ti/Al LMCs, the m-value was a little smaller than the monolithic Ti. However, the m-value (0.032) of the Al/Ti/Al LMCs was higher than the m-value calculated using the ROM (0.025) or the simple average value (0.029) of the monolithic Ti and monolithic Al. The discrepancy between the tested and calculated m-value (extra SRS) may be related to the extra activation of pyramidal and basal slip in the Ti layer (Fig. 7(a)) and multi-slip in the Al layer (Fig. 7(d)). Previous studies reported that the m-value was higher for Ti when the main deformation mode was basal slip compared with prismatic slip (Zhang et al., 2016). The high m-value reasonably explained the high post-necking elongation (~40%) in the Al/Ti/Al LMCs.

Based on the discussion above, we speculate that the improved ductility of the Al/Ti/Al LMCs compared with both monolithic Ti and monolithic Al may be caused by following two stages.

Stage I: with increasing applied tensile strain, necking tended to occur earlier in the Ti layer than the Al layer, as determined by the much higher uniform elongation of monolithic Al (~26%) than monolithic Ti (~12%). However, because of the constrained Al layer, necking in the Ti layer was delayed. Additionally, the constraint between the Ti layer and the Al layer was mutual. The necking in the Al layer in LMCs moved forward compared with monolithic Al. Hence, necking in the Al/Ti/Al LMCs (with uniform elongation ~22%) occurred later than for monolithic Ti but earlier than for monolithic Al, as indicated in Fig. 3.

Stage II: on further increasing the applied strain, necking also occurred in the Al layer. In monolithic Al, the strain concentrated rapidly in the necking area, thus leading to serious strain localization and fast cracking after necking (Ghosh, 1977). However, in the Al/Ti/Al LMCs, strain localization in the Al layer was delayed because of the constrained Ti layer. Constraint of the Al layer tends to cause faster strain localization in the Ti layer than that for the monolithic Ti. The extra activation of pyramidal and basal slipping may result in extra SRS in the Ti layer, which compensates for the effects of Al layer constraint. Therefore, the post-necking elongation (~40%) of Al/Ti/Al LMCs was nearly identical to that of monolithic Ti.

In Stage I, a higher uniform elongation was obtained in the Al/Ti/Al LMCs than for monolithic Ti. In Stage II, similar post-necking elongation was obtained. Therefore, through these two stages, improved fracture elongation could be obtained in the Al/Ti/Al LMCs compared with monolithic Ti. Compared with monolithic Al, the uniform elongation of the Al/Ti/Al LMCs reduced by a small amount (~4%), but the post-necking elongation increased markedly, which led to improved fracture elongation. It should be noted that there was a transition stage between Stage I and Stage II, in which necking occurred in the Ti layer but not in the Al layer. This transition stage existed over a small strain range and was hard to characterize; hence, it is not discussed further in the current study.

The Stage I, or delayed-necking mechanism, has been reported many times in previous studies on layered materials (Liu et al., 2011; Wang et al., 2019b). To validate the hypothesis for Stage II, after the applied tension, the distribution of $e_{L\text{-}TD}$ on the surface (Al layer) of the Al/Ti/Al LMCs was compared with that of monolithic Al, as shown in Fig. 15. It could be found that the strain localization in the Al layer of the Al/Ti/Al LMCs diffused over a larger distance compared with that in monolithic Al; thus, providing evidence for the slowing of the strain concentration.

It is worth noting that a high strain rate sensitivity is often assumed to be the key factor for achieving superplasticity (Arieli and Rosen, 1976). The strain rate sensitivity generally increased with increasing temperature (Rosen et al., 1999). Therefore, compared with the room temperature case, the enhanced ductility of Al/Ti/Al LMCs beyond that of the monolithic Ti and Al may be further improved by testing at high temperatures because of the enhanced strain rate sensitivity. The approach will be evaluated further by applying tension at various temperatures in future work.

6. Conclusions

In this work, thick Al/Ti/Al LMCs, with layer thicknesses ≥800 μm were fabricated via hot rolling bonding and annealing. Digital image correlation was used to analyze the strain distributions. Finite element simulations were performed to explore the effect of texture on the deformation of Al/Ti/Al. The slip trace method, based on ex-situ SEM and EBSD characterization, was used to investigate the effect of the layered structure on the deformation mechanism. The main conclusions can be summarized as follows.

(1) The tensile ductility of the thick Al/Ti/Al LMCs was better than that of the monolithic Ti and monolithic Al layers despite the annealing treatments. Extra strengthening above the rule of mixture was also observed.
(2) Interface affected zones with a width >150 μm were present near the Ti/Al interface, which was demonstrated to be mainly caused by a discrepancy r-value (texture induced anisotropic plastic flow) between the Ti layer and the Al layer. A wider IAZ was beneficial for improving the tensile ductility of the Al/Ti/Al LMCs.
(3) More pyramidal and basal slips were activated at the interface nearby region in the Ti layer, which may contribute to the enhanced strain-rate sensitivity of the Al/Ti/Al LMCs.
(4) The enhanced strain-rate sensitivity rather than strain hardening rate was assumed to play a crucial role in the extraordinary tensile ductility of the thick Al/Ti/Al LMCs.

Declaration of competing interest

The authors declare that they have no known competing financial interests or personal relationships that could have appeared to influence the work reported in this paper.

CRediT authorship contribution statement

Wenhuan Chen: Data curation, Investigation, Validation, Writing - original draft, Writing - review & editing. **Weijun He:** Conceptualization, Formal analysis, Investigation, Writing - review & editing, Funding acquisition, Supervision. **Zejun Chen:** Investigation, Formal analysis, Writing - review & editing. **Bin Jiang:** Validation, Writing - review & editing. **Qing Liu:** Funding acquisition, Supervision, Writing - review & editing.

Acknowledgments

The authors express their sincere thanks for the financial support from the National Natural Science Foundation of China (Projects 51971041, 51601023 and 51421001 and Natural Science Foundation of Chongqing (Projects No. cstc2019jcyj-msxmX0234). The Fundamental Research Funds for the Central Universities (No. 2020CDJDPT001) is greatly acknowledged.

Appendix A1

The detail information for the considered slip systems for Ti and Al are shown in Table A1.1.

Table A1.1
Possible slip systems considered in the slip trace analyses of Ti and Al.

Slip system number	Ti		Al
	Slip mode	Slip system	Slip system
1	Basal<a>	(0001)[-2110]	(111)[−110]
2		(0001)[-1-120]	(111)[−101]
3		(0001)[-12-10]	(111)[0–11]
4	Prismatic<a>	(01–10)[2-1-10]	(1–11)[110]
5		(10-10)[1–210]	(1–11)[−101]
6		(-1100)[11–20]	(1–11)[011]
7	Pyramidal<a>	(01–11)[2-1-10]	(-1-11)[−110]
8		(-1011)[-12-10]	(-1-11)[011]
9		(1–101)[-1-120]	(-1-11)[101]
10		(10–11)[-12-10]	(-111)[110]
11		(-1101)[-1-120]	(-111)[0–11]
12		(0–111)[2-1-10]	(-111)[101]
13	Pyramidal<c+a>	(01–11)[-1-123]	–
14		(01–11)[1–213]	–
15		(-1011)[2-1-13]	–
16		(-1011)[11–23]	–
17		(1–101)[-2113]	–
18		(1–101)[-12-13]	–

(*continued on next page*)

Table A1.1 (*continued*)

Slip system number	Ti		Al
	Slip mode	Slip system	Slip system
19		(10–11)[-1-123]	–
20		(10–11)[-2113]	–
21		(-1101)[2-1-13]	–
22		(-1101)[1–213]	–
23		(0–111)[11–23]	–
24		(0–111)[-12-13]	–

Fig. A1.1 illustrates the identification process of specific slip mode. As shown in Fig. A1.1(a), slip lines (marked by a blue line) are observed on the surface of Ti after 0.5% tensile deformation, which match well with the theoretical slip system 6. So, these slip lines are identified as prismatic slip 6(-1100)[11–20]. The first order pyramidal <a> and pyramidal <c+a> have the same slip planes {10–11}, so they produce the same trace. The slip system with the highest Schmid factor (SF) is chosen as the activated slip system. Taking grain 2 (Fig. A1.1(b)) as an example, among the three pyramidal slip systems (11/21/22), the pyramidal <c+a> 21(-1101)[2-1-13] has the greatest SF (0.30) and is selected as the activated slip system for the observed slip lines. In the same way, the basal slip 1(0001)[-2110] (SF = 0.47) is identified as the activated slip system for the observed slip lines in Fig. A1.1(c). For the identification of slip mode in Al, the same procedure as that for the basal slip in Ti is used. As indicated in Fig. A1.1(d), multi-slip systems are activated in one grain, including (1–11)[−101], (-1-11)[−110], and (−111)[0–11]. The specific SF calculation results are shown in Table A1.2.

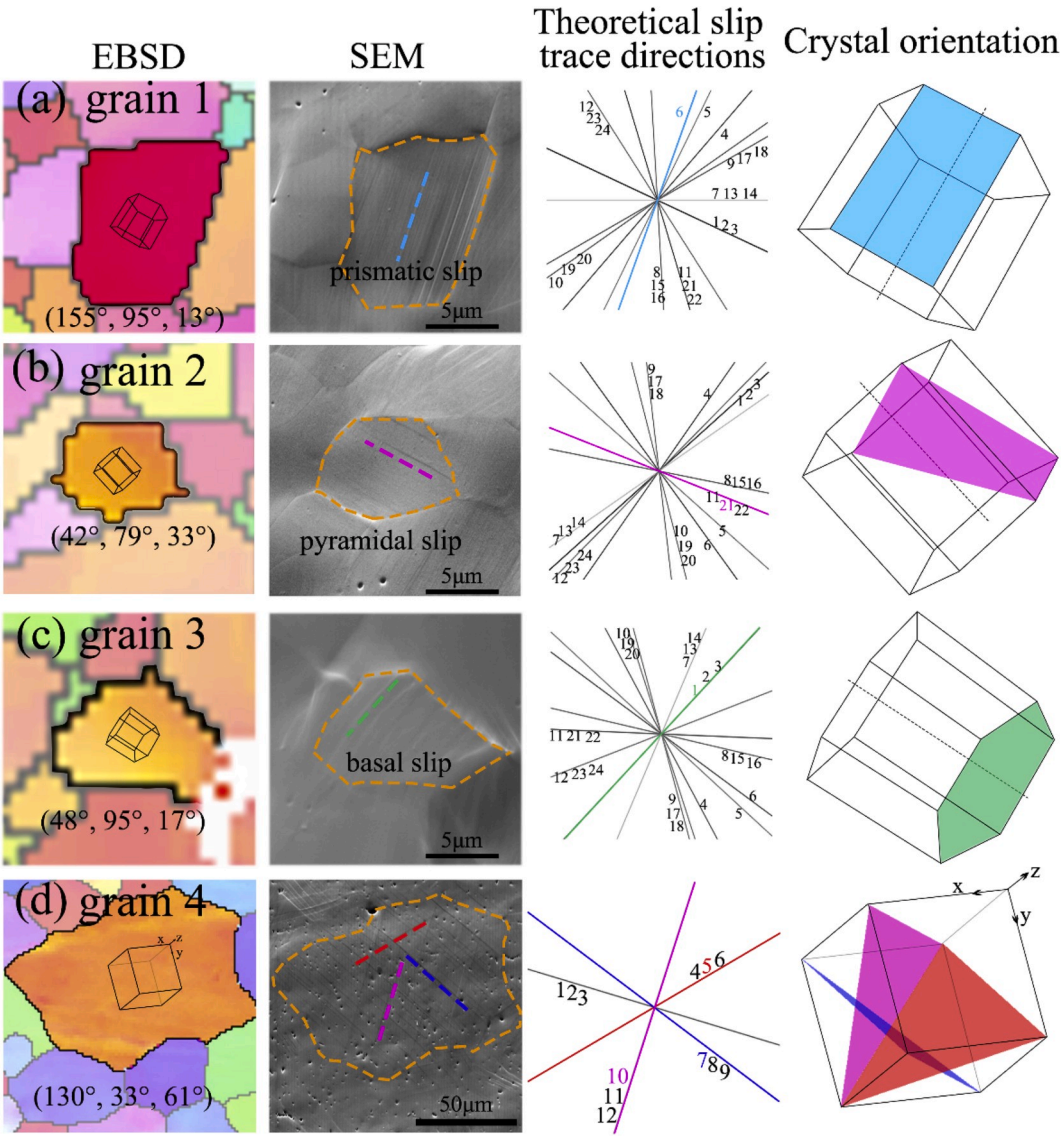

Fig. A1.1. Slip trace analyses on (a) prismatic slip, (b) pyramidal slip and (c) basal slip in Ti layer and (d) {111}<110> slip in Al layer based on SEM map, EBSD maps and the theoretical slip trace directions.

Table A1.2
Calculated SF of the slip systems in grain 1-3 (Ti) and grain 4 (Al). The bold SF represents the activated slip system for each grain.

Slip system number	Ti			Al
	grain 1	grain 2	Grain 3	grain 4
1/2/3	0.37/0.27/0.1	0.48/0.15/0.34	**0.47**/0.37/0.10	0.10/0.11/0.01
4	0.20	0.12	0.14	0.18
5	0.21	0.28	0.10	**0.37**
6	**0.40**	0.16	0.22	0.19
7/13/14	0.0/0.0/0.0	0.12/0.07/0.14	0.35/0.19/0.39	**0.48**/−/−
8/15/16	0.23/0.10/0.02	0.09/0.16/0.12	0.03/0.22/0.20	0.28/−/−
9/17/18	0.23/0.30/0.18	0.21/0.15/0.27	0.38/0.21/0.41	0.19/−/−
10/19/20	0.14/0.39/0.47	0.41/0.35/0.13	0.12/0.33/0.27	**0.39**/−/−
11/21/22	0.49/0.09/0.18	0.07/**0.30**/0.26	0.02/0.03/0.03	0.10/−/−
12/23/24	0.35/0.01/0.20	0.34/0.31/0.13	0.11/0.15/0.09	0.29/−/−

Appendix A2

The integration algorithmic aspects related to the displacement-based FE implementation are presented here. During an increment step [n, n+1], the trial stress is calculated as

$$\boldsymbol{\sigma}_{n+1}^{trial} = \boldsymbol{\sigma}_n + \mathbf{D} : \triangle\boldsymbol{\varepsilon}_n, \tag{A2.1}$$

where $\mathbf{D}$ denotes the fourth-order elasticity tensor. If $F(\boldsymbol{\sigma}_{n+1}^{trial}, \bar{\varepsilon}_n^p) \leq 0$, it is elastic deformation and $\sigma_{n+1} = \boldsymbol{\sigma}_{n+1}^{trial}$. If $F(\boldsymbol{\sigma}_{n+1}^{trial}, \bar{\varepsilon}_n^p) > 0$, there is plastic flow. The strain increment $\triangle\boldsymbol{\varepsilon}_n$ is composed of an elastic part $\triangle\boldsymbol{\varepsilon}_n^e$ and a plastic part $\triangle\boldsymbol{\varepsilon}_n^p$. The trial stress is then calculated by

$$\boldsymbol{\sigma}_{n+1}^{trial} = \boldsymbol{\sigma}_n + \mathbf{D} : \left(\triangle\boldsymbol{\varepsilon}_n - \triangle\boldsymbol{\varepsilon}_n^p \right). \tag{A2.2}$$

The evolution of the plastic strain is described by an associated flow rule:

$$\triangle\boldsymbol{\varepsilon}^p = \lambda \frac{\partial F}{\partial \boldsymbol{\sigma}}, \tag{A2.3}$$

where $\lambda \geq 0$ is the plastic multiplier.

For the plastic flow, the integration of the constitutive model leads to the following nonlinear system:

$$\begin{aligned} \sigma_{n+1} &= \sigma_{n+1}^{trial} - \lambda_n D : \frac{\partial F}{\partial \sigma} \\ F_{n+1} &= \Gamma\left(\sigma_{n+1}, \bar{\varepsilon}_n^p + \lambda_n\right) - \Pi\left(\bar{\varepsilon}_n^p + \lambda_n\right) = 0, \end{aligned} \tag{A2.4}$$

which is solved for σ_{n+1} and λ_n. The integration of Equation (A2.4) is performed by Newton–Raphson method, starting with $\boldsymbol{\sigma}_{n+1}^{initial} = \boldsymbol{\sigma}_{n+1}^{trial}$ and $\lambda_n^{initial} = 0$. When $F(\sigma_{n+1}, \bar{\varepsilon}_p) = 0$ is satisfied within a specified tolerance (for example 10^{-6}), stress and strain are updated.

In Equation (A2.4), the differential $\frac{\partial F}{\partial \boldsymbol{\sigma}}$ is calculated by numerical method as

$$\frac{\partial F}{\partial \boldsymbol{\sigma}} = \frac{F(\boldsymbol{\sigma} + \triangle\boldsymbol{\sigma}) - F(\boldsymbol{\sigma})}{\triangle\boldsymbol{\sigma}} \tag{A2.5}$$

where $\triangle\boldsymbol{\sigma}$ is a small stress increment.

The detail integration algorithmic of the constitutive model is also referred to reference (Plunkett et al., 2006).

Appendix A3

In order to determine the anisotropy parameters involved in the yield criterion, the error function is minimized. For in-plane tension at theta (θ) angle with respect to the rolling direction, as shown in Fig. A3.1, the corresponding stress tensor $\boldsymbol{\sigma}'$ expressed in specimen frame (x_1', x_2' system in Fig. A3.1) is

$$\boldsymbol{\sigma}' = \sigma_\theta^T \begin{bmatrix} 1 & 0 & 0 \\ 0 & 0 & 0 \\ 0 & 0 & 0 \end{bmatrix}, \tag{A3.1}$$

where σ_θ^T is the flow stress in the corresponding direction. Then, the corresponding tensor $\boldsymbol{\sigma}$ expressed in material frame (x_1, $x_2$system in Fig. A3.1) can be represented as

$$\boldsymbol{\sigma} = R^{-1}\boldsymbol{\sigma}' R = \sigma_\theta^T \begin{bmatrix} \cos^2\theta & -\cos\theta\sin\theta & 0 \\ -\cos\theta\sin\theta & \sin^2\theta & 0 \\ 0 & 0 & 0 \end{bmatrix}, \tag{A3.2}$$

where R is the rotation matrix from material frame to specimen frame,

$$R = \begin{bmatrix} \cos\theta & -\sin\theta & 0 \\ \sin\theta & \cos\theta & 0 \\ 0 & 0 & 1 \end{bmatrix}. \tag{A3.3}$$

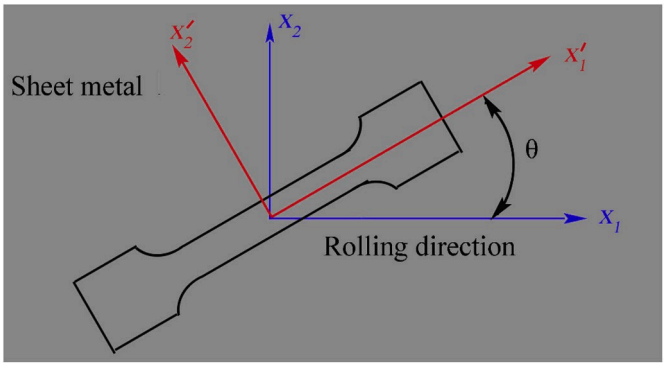

Fig. A3.1. Orientation of the tensile specimen with the rolling direction of sheet.

Thus, the deviator stress **S** in material frame in the form of column vector is

$$S = \sigma_\theta^T\left[\left(\cos^2\theta - 1/3\right)\ \left(\sin^2\theta - 1/3\right)\ -1/3\ -\cos\theta\sin\theta\ 0\ 0\right]^T = \sigma_\theta^T S_\theta^T. \tag{A3.4}$$

The tensile flow stress σ_θ^T normalized by the tension flow stress along the rolling direction (σ_0^T) is given by

$$\frac{\sigma_\theta^T}{\sigma_0^T} = \left(\frac{F\left(\mathbf{S}_0^T\right)}{F\left(\mathbf{S}_\theta^T\right)}\right)^{1/a}. \tag{A3.5}$$

Furthermore, the r-value is defined as the width-to-thickness strain ratio during uniaxial test. Since the plastic potential is assumed to coincide with the yield function, the plastic strain increments are derived from the plastic potential according to the associated flow rule. Therefore, the plastic strain ratio tensor in material frame is

$$\dot{\boldsymbol{\varepsilon}}^p = \dot{\lambda}\begin{bmatrix} \frac{\partial F}{\partial\sigma_{11}} & \frac{\partial F}{\partial\sigma_{12}} & \frac{\partial F}{\partial\sigma_{13}} \\ \frac{\partial F}{\partial\sigma_{21}} & \frac{\partial F}{\partial\sigma_{22}} & \frac{\partial F}{\partial\sigma_{23}} \\ \frac{\partial F}{\partial\sigma_{31}} & \frac{\partial F}{\partial\sigma_{32}} & \frac{\partial F}{\partial\sigma_{33}} \end{bmatrix}. \tag{A3.6}$$

For in-plane tension at θ degrees with respect to the rolling direction, the plastic strain ratio tensor in specimen frame is

$$\dot{\varepsilon}_\theta^{'p} = R\dot{\varepsilon}^p R^{-1}. \tag{A3.7}$$

Let r_θ denotes the r-value tensile loading in direction θ degrees with respect to the rolling direction. Hence,

$$r_\theta = \frac{\frac{df}{d\sigma_{2'2'}}}{\frac{df}{d\sigma_{3'3'}}} = -\frac{\sin^2\theta\frac{\partial F}{\partial\sigma_{11}} - \sin(2\theta)\frac{\partial F}{\partial\sigma_{12}} + \cos^2\theta\frac{\partial F}{\partial\sigma_{22}}}{\frac{\partial F}{\partial\sigma_{11}} + \frac{\partial F}{\partial\sigma_{22}}}, \tag{A3.8}$$

where f is the yield function in specimen frame and F is the yield function in material frame.

In the present work, anisotropy parameters are identified at different strain levels, 0.002, 0.012, 0.032 … 0.252. Based on the identified anisotropy parameters, the evolution of yield surface on Pi-plane are shown in Fig. A3.2.

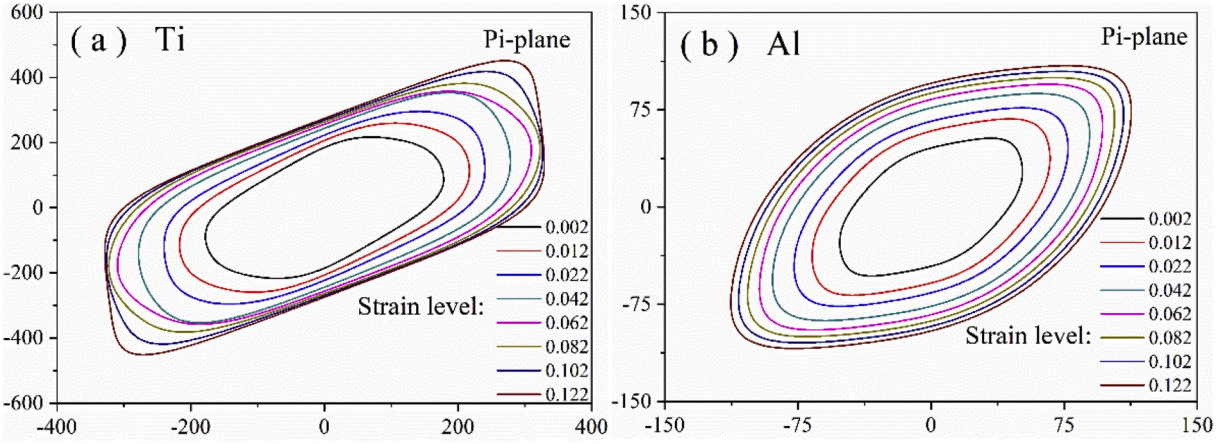

Fig. A3.2. Typical yielding locus on Pi-plane for (a) Ti and (b) Al at different strains.

References

Arieli, A., Rosen, A., 1976. Measurements of the strain rate sensitivity coefficient in superplastic Ti6Al4V alloy. Scripta Metall. 10, 471–475.

Ashby, M.F., 1970. The deformation of plastically non-homogeneous materials. Philos. Mag. A 21, 399–424.

Baral, M., Hama, T., Knudsen, E., Korkolis, Y.P., 2018. Plastic deformation of commercially-pure titanium: experiments and modeling. Int. J. Plast. 105, 164–194.

Bardella, L., 2006. A deformation theory of strain gradient crystal plasticity that accounts for geometrically necessary dislocations. J. Mech. Phys. Solid. 54, 128–160.

Barkia, B., Doquet, V., Couzinié, J.P., Guillot, I., Héripré, E., 2015. In situ monitoring of the deformation mechanisms in titanium with different oxygen contents. Mater. Sci. Eng., A 636, 91–102.

Chen, T., Yuan, R., Beyerlein, I.J., Zhou, C., 2020. Predicting the size scaling in strength of nanolayered materials by a discrete slip crystal plasticity model. Int. J. Plast. 124, 247–260.

Chen, W.H., He, W.J., Chen, Z.J., Zhou, Z., Liu, Q., 2019. Effect of wavy profile on the fabrication and mechanical properties of Al/Ti/Al composites prepared by rolling bonding: experiments and finite element simulations. Adv. Eng. Mater. 21, 1900637.

Cheng, Z., Zhou, H., Lu, Q., Gao, H., Lu, L., 2018. Extra strengthening and work hardening in gradient nanotwinned metals. Science 362, 559–566.

Du, Y., Fan, G., Yu, T., Hansen, N., Geng, L., Huang, X., 2016. Laminated Ti-Al composites: processing, structure and strength. Mater. Sci. Eng., A 673, 572–580.

Fang, T.H., Li, W.L., Tao, N.R., Lu, K., 2011. Revealing extraordinary intrinsic tensile plasticity in gradient nano-grained copper. Science 331, 1587–1590.

Fu, Z., Zhang, Z., Meng, L., Shu, B., Zhu, Y., Zhu, X., 2018. Effect of strain rate on mechanical properties of Cu/Ni multilayered composites processed by electrodeposition. Mater. Sci. Eng., A 726, 154–159.

Ghosh, A.K., 1977. The influence of strain hardening and strain rate sensitivity on sheet metal forming. J. Eng. Mater. Technol. 99, 264–274.

Ghosh, M., Miroux, A., Kestens, L.A.I., 2015. Correlating r-value and through thickness texture in Al–Mg–Si alloy sheets. J. Alloys Compd. 619, 585–591.

Gurtin, M., Needleman, A., 2005. Boundary conditions in small-deformation, single-crystal plasticity that account for the Burgers vector. J. Mech. Phys. Solid. 53, 1–31.

Habibi, M.K., Samaei, A.T., Gheshlaghi, B., Lu, J., Lu, Y., 2015. Asymmetric flexural behavior from bamboo's functionally graded hierarchical structure: underlying mechanisms. Acta Biomater. 16, 178–186.

Hasan, M.N., Liu, Y.F., An, X.H., Gu, J., Song, M., Cao, Y., Li, Y.S., Zhu, Y.T., Liao, X.Z., 2019. Simultaneously enhancing strength and ductility of a high-entropy alloy via gradient hierarchical microstructures. Int. J. Plast. 123, 178–195.

Heinemann, F., Launspach, M., Gries, K., Fritz, M., 2011. Gastropod nacre: structure, properties and growth — biological, chemical and physical basics. Biophys. Chem. 153, 126–153.

Huang, C.X., Wang, Y.F., Ma, X.L., Yin, S., Höppel, H.W., Göken, M., Wu, X.L., Gao, H.J., Zhu, Y.T., 2018a. Interface affected zone for optimal strength and ductility in heterogeneous laminate. Mater. Today 21, 713–719.

Huang, M., 2019. Study on Deformation and Fracture Behavior of Layered Ti/Al Metal Composites. Harbin Institute of Technology.

Huang, M., Fan, G.H., Geng, L., Cao, G.J., Du, Y., Wu, H., Zhang, T.T., Kang, H.J., Wang, T.M., Du, G.H., Xie, H.L., 2016. Revealing extraordinary tensile plasticity in layered Ti-Al metal composite. Sci. Rep. 6, 38461.

Huang, M., Xu, C., Fan, G., Maawad, E., Gan, W., Geng, L., Lin, F., Tang, G., Wu, H., Du, Y., Li, D., Miao, K., Zhang, T., Yang, X., Xia, Y., Cao, G., Kang, H., Wang, T., Xiao, T., Xie, H., 2018b. Role of layered structure in ductility improvement of layered Ti-Al metal composite. Acta Mater. 153, 235–249.

Inagaki, H., 1992. Texture and mechanical anisotropy in cold rolled and annealed pure Ti sheets. Zeitschrift fuer Metallkunde (Germany) 83, 40–46.

Inoue, J., Nambu, S., Ishimoto, Y., Koseki, T., 2008. Fracture elongation of brittle/ductile multilayered steel composites with a strong interface. Scripta Mater. 59, 1055–1058.

Jiao, D., Liu, Z., Zhang, Z., Zhang, Z., 2015. Intrinsic hierarchical structural imperfections in a natural ceramic of bivalve shell with distinctly graded properties. Sci. Rep. 5, 12418.

Jin, J.E., Lee, Y.K., 2012. Effects of Al on microstructure and tensile properties of C-bearing high Mn TWIP steel. Acta Mater. 60, 1680–1688.

Kim, I., Hong, S., 2013. Roll-bonded tri-layered Mg/Al/stainless steel clad composites and their deformation and fracture behavior. Metall. Mater. Trans. A 44, 3890–3900.

Kim, J.G., Baek, S.M., Lee, H.H., Chin, K.-G., Lee, S., Kim, H.S., 2018. Suppressed deformation instability in the twinning-induced plasticity steel-cored three-layer steel sheet. Acta Mater. 147, 304–312.

Kuroda, M., Tvergaard, V., 2008. On the formulations of higher-order strain gradient crystal plasticity models. J. Mech. Phys. Solid. 56, 1591–1608.

Kuwabara, T., Mori, T., Asano, M., Hakoyama, T., Barlat, F., 2017. Material modeling of 6016-O and 6016-T4 aluminum alloy sheets and application to hole expansion forming simulation. Int. J. Plast. 93, 164–186.

Lesuer, D.R., Syn, C.K., Sherby, O.D., Wadsworth, J., Lewandowski, J.J., Hunt, W.H., 1996. Mechanical behaviour of laminated metal composites. Int. Mater. Rev. 41, 169–197.

Li, D., Ghosh, A., 2003. Tensile deformation behavior of aluminum alloys at warm forming temperatures. Mater. Sci. Eng., A 352, 279–286.

Li, J., Wang, S., Mao, Q., Huang, Z., Li, Y., 2019a. Soft/hard copper/bronze laminates with superior mechanical properties. Mater. Sci. Eng., A 756, 213–218.

Li, J., Weng, G.J., Chen, S., Wu, X., 2017. On strain hardening mechanism in gradient nanostructures. Int. J. Plast. 88, 89–107.

Li, S., Zhao, Q., Liu, Z., Li, F., 2018. A review of texture evolution mechanisms during deformation by rolling in aluminum alloys. J. Mater. Eng. Perform. 27, 3350–3373.
Li, Z., Voisin, T., McKeown, J.T., Ye, J., Braun, T., Kamath, C., King, W.E., Wang, Y.M., 2019b. Tensile properties, strain rate sensitivity, and activation volume of additively manufactured 316L stainless steels. Int. J. Plast. 120, 395–410.
Liang, F., Luo, X.M., Zhang, G.P., 2019. Interface-coupling-dependent mechanical behaviors of sandwich-structured Ni/Cu/Ni composites. Mater. Sci. Eng., A 743, 436–444.
Lin, Y., Pan, J., Zhou, H.F., Gao, H.J., Li, Y., 2018. Mechanical properties and optimal grain size distribution profile of gradient grained nickel. Acta Mater. 153, 279–289.
Liu, H.S., Zhang, B., Zhang, G.P., 2011. Delaying premature local necking of high-strength Cu: a potential way to enhance plasticity. Scripta Mater. 64, 13–16.
Liu, Z., Meyers, M.A., Zhang, Z., Ritchie, R.O., 2017. Functional gradients and heterogeneities in biological materials: design principles, functions, and bioinspired applications. Prog. Mater. Sci. 88, 467–498.
Lu, K., 2010. The future of metals. Science 328, 319–320.
Lu, K., 2014. Making strong nanomaterials ductile with gradients. Science 345, 1455–1456.
Lu, K., Lu, L., Suresh, S., 2009. Strengthening materials by engineering coherent internal boundaries at the nanoscale. Science 324, 349–352.
Lu, X., Zhao, J., Wang, Z., Gan, B., Zhao, J., Kang, G., Zhang, X., 2020. Crystal plasticity finite element analysis of gradient nanostructured TWIP steel. Int. J. Plast. 130, 102703.
Ma, X., Huang, C., Moering, J., Ruppert, M., Höppel, H.W., Göken, M., Narayan, J., Zhu, Y., 2016. Mechanical properties of copper/bronze laminates: role of interfaces. Acta Mater. 116, 43–52.
Ma, X.L., Huang, C.X., Xu, W.Z., Zhou, H., Wu, X.L., Zhu, Y.T., 2015. Strain hardening and ductility in a coarse-grain/nanostructure laminate material. Scripta Mater. 103, 57–60.
Mompiou, F., Legros, M., Boé, A., Coulombier, M., Raskin, J.P., Pardoen, T., 2013. Inter- and intragranular plasticity mechanisms in ultrafine-grained Al thin films: an in situ TEM study. Acta Mater. 61, 205–216.
Nizolek, T., Beyerlein, I.J., Mara, N.A., Avallone, J.T., Pollock, T.M., 2016. Tensile behavior and flow stress anisotropy of accumulative roll bonded Cu-Nb nanolaminates. Appl. Phys. Lett. 108, 051903.
Orozco-Caballero, A., Li, F., Esqué-de los Ojos, D., Atkinson, M.D., Quinta da Fonseca, J., 2018. On the ductility of alpha titanium: the effect of temperature and deformation mode. Acta Mater. 149, 1–10.
Park, H.K., Ameyama, K., Yoo, J., Hwang, H., Kim, H.S., 2018. Additional hardening in harmonic structured materials by strain partitioning and back stress. Mater. Res. Lett. 6, 261–267.
Plunkett, B., Cazacu, O., Barlat, F., 2008. Orthotropic yield criteria for description of the anisotropy in tension and compression of sheet metals. Int. J. Plast. 24, 847–866.
Plunkett, B., Lebensohn, R.A., Cazacu, O., Barlat, F., 2006. Anisotropic yield function of hexagonal materials taking into account texture development and anisotropic hardening. Acta Mater. 54, 4159–4169.
Qin, L., Wang, J., Wu, Q., Guo, X., Tao, J., 2017. In-situ observation of crack initiation and propagation in Ti/Al composite laminates during tensile test. J. Alloys Compd. 712, 69–75.
Rosen, R.S., Paddon, S.P., Kassner, M.E., 1999. The variation of the yield stress of Ti alloys with strain rate at high temperatures. J. Mater. Eng. Perform. 8, 361–367.
Seok, M.Y., Lee, J.A., Lee, D.H., Ramamurty, U., Jang, J.I., 2016. Decoupling the contributions of constituent layers to the strength and ductility of a multi-layered steel. Acta Mater. 121, 164–172.
Shao, C.W., Zhang, P., Zhu, Y.K., Zhang, Z.J., Tian, Y.Z., Zhang, Z.F., 2018. Simultaneous improvement of strength and plasticity: additional work-hardening from gradient microstructure. Acta Mater. 145, 413–428.
Singh, A.K., Schwarzer, R.A., 2000. Texture and anisotropy of mechanical properties in titanium and its alloys. Int. J. Mater. Res. 91, 702–716.
Sitarama Raju, K., Subramanya Sarma, V., Kauffmann, A., Hegedűs, Z., Gubicza, J., Peterlechner, M., Freudenberger, J., Wilde, G., 2013. High strength and ductile ultrafine-grained Cu–Ag alloy through bimodal grain size, dislocation density and solute distribution. Acta Mater. 61, 228–238.
Tanaka, Y., Kondo, M., Miyazaki, N., Ueji, R., 2010. Deformation behavior of pure titanium at a wide range of strain rates. J. Phys. Conf. Ser. 240.
Tertuliano, O.A., Greer, J.R., 2016. The nanocomposite nature of bone drives its strength and damage resistance. Nat. Mater. 15, 1195.
Verdier, M., Huang, H., Spaepen, F., Embury, J.D., Kung, H., 2006. Microstructure, indentation and work hardening of Cu/Ag multilayers. Philos. Mag. A 86, 5009–5016.
Wang, J.X., Zecevic, M., Knezevic, M., Beyerlein, I.J., 2020. Polycrystal plasticity modeling for load reversals in commercially pure titanium. Int. J. Plast. 125, 294–313.
Wang, L., Shi, Y., Zhang, Y., Li, M., 2018a. High tensile ductility and strength in a gradient structured Zr. Mater. Lett. 228, 500–503.
Wang, Y., He, W.J., Liu, N., Chapuis, A., Luan, B.F., Liu, Q., 2018b. Effect of pre-annealing deformation on the recrystallized texture and grain boundary misorientation in commercial pure titanium. Mater. Char. 136, 1–11.
Wang, Y.F., Huang, C.X., Wang, M.S., Li, Y.S., Zhu, Y.T., 2018c. Quantifying the synergetic strengthening in gradient material. Scripta Mater. 150, 22–25.
Wang, Y.F., Wang, M., Yin, K., Huang, A., Li, Y., Huang, C., 2019a. Yielding and fracture behaviors of coarse-grain/ultrafine-grain heterogeneous-structured copper with transitional interface. T. Nonferr. Metal. Soc. 29, 588–594.
Wang, Y.F., Wang, M.S., Fang, X.T., Guo, F.J., Liu, H.Q., Scattergood, R.O., Huang, C.X., Zhu, Y.T., 2019b. Extra strengthening in a coarse/ultrafine grained laminate: role of gradient interfaces. Int. J. Plast. 123, 196–207.
Wang, Z.J., Zhai, L., Ma, M., Yuan, H., Liu, W.C., 2015. Microstructure, texture and mechanical properties of Al/Al laminated composites fabricated by hot rolling. Mater. Sci. Eng., A 644, 194–203.
Wu, H., Fan, G.H., Huang, M., Geng, L., Cui, X.P., Xie, H.L., 2017. Deformation behavior of brittle/ductile multilayered composites under interface constraint effect. Int. J. Plast. 89, 96–109.
Wu, X., Zhu, Y., 2017. Heterogeneous materials: a new class of materials with unprecedented mechanical properties. Mater. Res. Lett. 5, 527–532.
Wu, X.L., Jiang, P., Chen, L., Yuan, F., Zhu, Y., 2014a. Extraordinary strain hardening by gradient structure. Proc. Natl. Acad. Sci. Unit. States Am. 111, 7197.
Wu, X.L., Jiang, P., Chen, L., Zhang, J.F., Yuan, F.P., Zhu, Y.T., 2014b. Synergetic strengthening by gradient structure. Mater. Res. Lett. 2, 185–191.
Wu, Y., Feng, B., Xin, Y., Hong, R., Yu, H., Liu, Q., 2015. Microstructure and mechanical behavior of a Mg AZ31/Al 7050 laminate composite fabricated by extrusion. Mater. Sci. Eng., A 640, 454–459.
Yang, H., Li, H., Ma, J., Wei, D., Chen, J., Fu, M.W., 2020. Temperature dependent evolution of anisotropy and asymmetry of α-Ti in thermomechanical working: characterization and modeling. Int. J. Plast. 127, 102650.
Yang, X., Ma, X., Moering, J., Zhou, H., Wang, W., Gong, Y., Tao, J., Zhu, Y., Zhu, X., 2015. Influence of gradient structure volume fraction on the mechanical properties of pure copper. Mater. Sci. Eng., A 645, 280–285.
Yilmaz, E.D., Schneider, G.A., Swain, M.V., 2015. Influence of structural hierarchy on the fracture behaviour of tooth enamel. Philos. Trans. R. Soc. A 373.
Yin, Z., Yang, X., Ma, X., Moering, J., Yang, J., Gong, Y., Zhu, Y., Zhu, X., 2016. Strength and ductility of gradient structured copper obtained by surface mechanical attrition treatment. Mater. Des. 105, 89–95.
Zhang, Z., Jun, T.S., Britton, T.B., Dunne, F.P.E., 2016. Intrinsic anisotropy of strain rate sensitivity in single crystal alpha titanium. Acta Mater. 118, 317–330.
Zhao, J., Lu, X., Yuan, F., Kan, Q., Qu, S., Kang, G., Zhang, X., 2020. Multiple mechanism based constitutive modeling of gradient nanograined material. Int. J. Plast. 125, 314–330.
Zhou, H., Huang, C., Sha, X., Xiao, L., Ma, X., Höppel, H.W., Göken, M., Wu, X., Ameyama, K., Han, X., Zhu, Y., 2019. In-situ observation of dislocation dynamics near heterostructured interfaces. Mater. Res. Lett. 7, 376–382.

Zhu, G.M., Wang, L.Y., Zhou, H., Wang, J.H., Shen, Y., Tu, P., Zhu, H., Liu, W., Jin, P.P., Zeng, X.Q., 2019a. Improving ductility of a Mg alloy via non-basal < a > slip induced by Ca addition. Int. J. Plast. 120, 164–179.
Zhu, H., Sun, W., Kong, F., Wang, X., Song, Z., Chen, Y., 2019b. Interfacial characteristics and mechanical properties of TiAl/Ti6Al4V laminate composite (LMC) fabricated by vacuum hot pressing. Mater. Sci. Eng., A 742, 704–711.
Zhu, L., Lu, J., 2012. Modelling the plastic deformation of nanostructured metals with bimodal grain size distribution. Int. J. Plast. 30–31, 166–184.